DISSERTATION FOR A DEGREE OF
DOCTOR OF PHILOSOPHY IN SCIENCE
TOKYO METROPOLITAN UNIVERSITY

TITLE: **Studies on physical properties and lattice anharmonicity in $BiCh_2$-based layered compounds**

AUTHOR：Fysol Ibna Abbas

EXAMINED BY

Examiner in chief	Yoshikazu Mizuguchi, Associate Professor
Examiner	Rei Kurita, Professor
Examiner	Kazumasa Hattori, Associate Professor

QUALIFIED BY THE GRADUATE SCHOOL OF SCIENCE
TOKYO METROPOLITAN UNIVERSITY

Dean

Date

Doctoral thesis

Studies on physical properties and lattice anharmonicity in $BiCh_2$-based layered compounds

Fysol Ibna Abbas

Department of Physics
Tokyo Metropolitan University
2024. 02. 16

Abstract

Fysol Ibna Abbas

Layered compounds have attracted much attention because of the emergence of various exotic physical properties and functionalities. Among them, $BiCh_2$-based layered compounds have been studied as superconducting and thermoelectric materials. The mostly-studied parent phase $LaOBiS_2$ is a semiconductor, and electron carriers are generated by F substitution for the O site in $La(O,F)BiS_2$. The electron-doped $La(O,F)BiS_2$ exhibits superconductivity at low temperatures, but the system does not show bulk superconductivity, which is caused by huge local disorder (random displacement from the average atomic position) at in-plane S1 site. To induce bulk superconductivity, in-plane chemical pressure (CP) effect, which reduces in-plane S1 disorder (amplitude of in-plane atomic displacement parameter, U_{11}), is essential. The in-plane CP can be applied by RE-site substitution with smaller RE^{3+} or Se substitution for the S site. The in-plane CP effect is also important for enhancing thermoelectric performance in $LaOBi(S,Se)_2$. By Se substitution, in-plane S1 disorder is suppressed, and carrier mobility is largely enhanced, which results in the enhancement of power factor $PF = S^2/\rho$ where S and ρ are Seebeck coefficient and electrical resistivity, respectively. Furthermore, the in-plane CP by Se substitution in $LaOBi(S,Se)_2$ results in the suppression of thermal conductivity κ, resulting the improvement of dimensionless figure-of-merit $ZT = S^2T/\rho\kappa$. From inelastic neutron scattering and phonon calculations, the correlation between κ and the optical phonon energy corresponding to Bi large-amplitude vibration along the c-axis have been proposed.

In both superconducting and thermoelectric compositions of $RE(O,F)Bi(S,Se)_2$, the effect of in-plane CP on the in-plane crystal structure including Ch1-site (Ch1: in-plane chalcogen site) and Bi-Ch1 disorder has been well studied in various compositions, and the suppression of the in-plane S1 disorder is essential for the emergence of bulk superconductivity and high thermoelectric PF. However, the study on the Bi large-amplitude vibration along the c-axis has not been studied in detail particularly for superconductor compositions. To deeper the understanding of the physical properties of $BiCh_2$-based compounds, investigation on the effect of in-plane CP on the Bi vibration are important. In this study, we investigate the effects

of in-plane CP on the phonons and anharmonicity in RE(O,F)Bi(S,Se)$_2$ by analyzing specific heat and estimating Grüneisen parameter.

In materials with low-energy optical phonons, for example, the rattling mode in caged compounds, the contribution of the optical phonons appears in low-temperature specific heat. As mentioned above, Bi large-amplitude vibration along the *c*-axis is observed in LaOBi(S,Se)$_2$, and the optical phonon energy is about 7 meV. Therefore, the low-energy optical phonon can be detected by specific heat. In this study, we analyzed phonons using specific heat data for thermoelectric compositions of $LaOBiS_2$ and LaOBiSSe and superconducting compositions of $LaO_{0.5}F_{0.5}BiS_2$ and $LaO_{0.5}F_{0.5}BiSSe$. For all the cases, the model with two Debye models and three Einstein models resulted in reasonable fitting of the temperature dependence of lattice specific heat C_{lat}/T^3. For $LaOBiS_2$ and LaOBiSSe, the oscillator number strength (n) for the optical phonon with an Einstein temperature $\theta_E \sim 70$ K (7 meV) clearly increases by Se substitution, which generates positive in-plane CP. Furthermore, a similar trend, an increase in n for the Einstein mode with $\theta_E \sim 70$ K, is observed by Se substitution in $LaO_{0.5}F_{0.5}BiS_2$ and $LaO_{0.5}F_{0.5}BiSSe$. Those results suggest that the in-plane CP stabilizes the optical phonon modes corresponding to the Bi large-amplitude vibration along the *c*-axis.

Because low-energy optical phonon would contribute to the enhancement of anharmonicity in materials, we estimated the effects of in-plane CP on lattice anharmonicity by estimating Grüneisen parameter. For LaOBi(S,Se)$_2$, $LaO_{0.5}F_{0.5}Bi(S,Se)_2$, and RE(O,F)$BiS_2$, the Grüneisen parameter increases with increasing in-plane CP. Therefore, in-plane CP in BiS_2-based RE(O,F)Bi(S,Se)$_2$ results in the stabilization of Bi *c*-axis vibration and the enhancement of lattice anharmonicity. The scenario proposed in this study will be useful for further understanding of the physical properties and functionalities in layered $BiCh_2$-based compounds.

Contents

1. Introduction for $BiCh_2$-based compounds

In this study, we investigated the effects of in-plane chemical pressure (CP) on Bi large-amplitude vibration along the *c*-axis and lattice anharmonicity in $BiCh_2$-based (Ch: S, Se) layered compounds. In the $BiCh_2$-based system, superconductivity is induced, and high thermoelectric performance is observed when in-plane CP on the in-plane Bi-Ch bonds is increased. In this introduction part, we mainly explain the crystal structure, carrier doping, and in-plane CP effects. The basis of superconductors and thermoelectric materials is written in Appendix.

1.1 Crystal structure and superconductivity in BiS_2-based compounds

The layer superconductors, $Bi_4O_4S_3$ and $La(O,F)BiS_2$, with BiS_2-type conducting layers, were discovered in 2012 [1–3]. The $Bi_4O_4S_3$ phase was an unknown phase in the material database. Therefore, the crystal structure was determined by Rietveld refinement and molecular dynamics calculation [1]. The crystal structure of $Bi_4O_4S_3$ determined bystructural analysis is depicted in Fig. 1(a). The crystal structure of the $Bi_4O_4S_3$ superconductor is composed of alternate stacks of a BiS_2 superconducting double layer and the $Bi_4O_4(SO_4)_{0.5}$ blocking layer [1]. The space group of $Bi_4O_4S_3$ is tetragonal $I4/mmm$ (No. 139). Electronic band calculation suggested that the conduction band is mainly composed of Bi $6p_x$ and $6p_y$ orbitals hybridized with S 3p orbitals; hence, the BiS_2 layer acts as a conducting layer; more precisely, the BiS planes are main contributor on electronic conduction [1]. The electron carriers are generated by the SO_4 defects. The temperature dependences of specific heat, resistivity, and magnetic susceptibility are shown in Figs. 1(b–d). T_c for $Bi_4O_4S_3$ observed oy bulk measurements is 4–5 K [4], but the feature of an opening of superconducting gap was observed in scanning tunneling spectroscopy (STS) in $Bi_4O_4S_3$ up to 14 K by spectroscopy [5], which suggested the possibility of a higher T_c in this system.

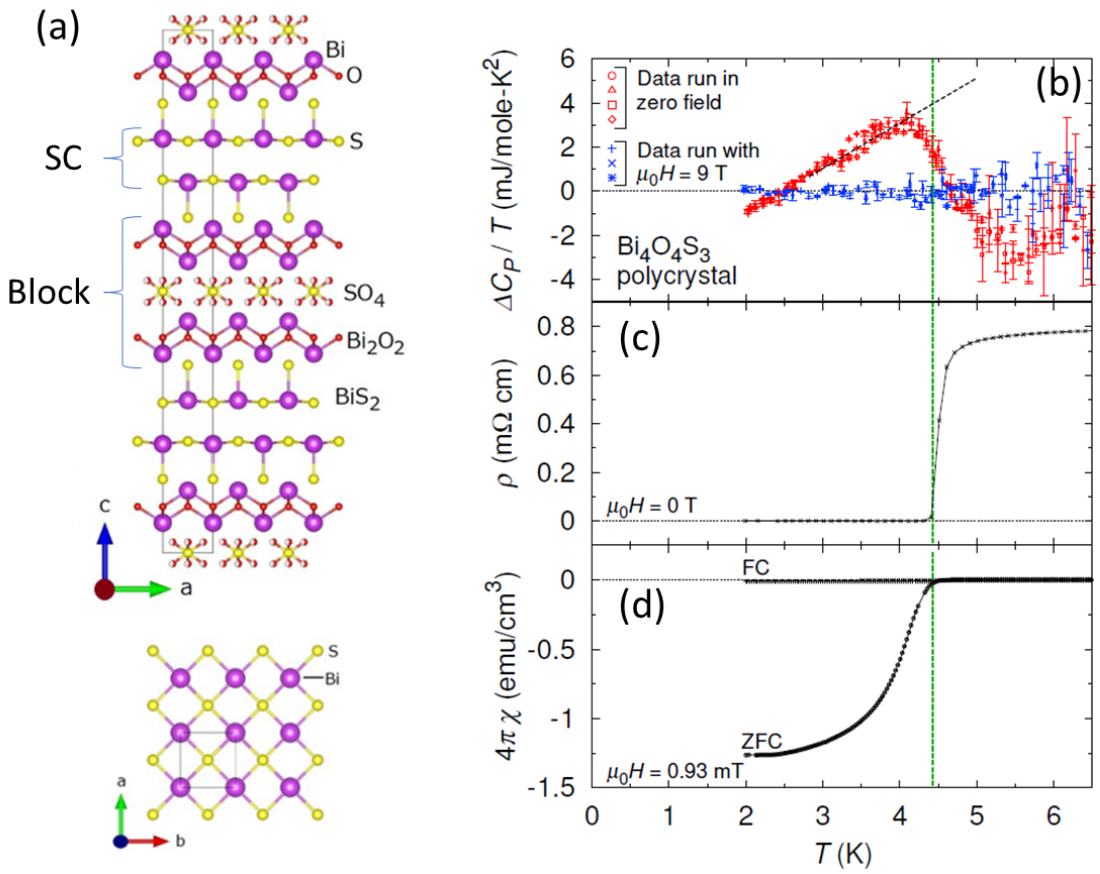

Figure 1. (a) Crystal structure images of $Bi_4O_4S_3$. (b–d) Temperature dependences of (b) specific heat, (c) electrical resistivity, and (d) magnetic susceptibility of $Bi_4O_4S_3$. Partly reproduced from Refs. 1 and 4.

The $REOBiS_2$-based (RE: La, Ce, Pr, Nd, Sm, Yb, Y, Bi) phases of the BiS_2-based superconductors have received the most attention because of their flexible structure [Fig. 2(a)] and carrier doping by various methods. The crystal structure of $REOBiS_2$ is the alternate stacks of a BiS_2 layer and a REO blocking layer, and the space group is tetragonal *P*4/*nmm* (No. 129). $LaO_{1-x}F_xBiS_2$ was the first compound in which superconductivity in the $REOBiS_2$-based compound was reported [2]. For $x = 0$, the obtained parent phase is a semiconductor with a band gap [6,7]. Superconductivity is induced in the electron-doped phases with F substitution. This demonstrates that superconducting states can be induced by partial substitution of F^- for O^{2-} in the $LaO_{1-x}F_xBiS_2$ system.

However, it was found that the polycrystalline samples of electron-doped $LaO_{1-x}F_xBiS_2$ do not exhibit conventional metallic behavior, which is generally understood as a decrease in resistivity with decreasing temperature. It was found that doped carriers are weakly localized,

and that resulted in the localized (semiconductor-like) behavior in the temperature dependence of resistivity as shown in Fig. 2(b) [3,8]. In addition, the shielding volume fraction in the magnetic susceptibility data is quite tiny in the temperature dependence of susceptibility data as shown in Fig. 2(c). Therefore, $LaO_{0.5}F_{0.5}BiS_2$ is categorized into a filamentary superconductor (in other words, trace superconductivity or weak superconductivity). Later, it was found that the in-plane CP effects are essential for the emergence of bulk superconductivity in the system [9], which will be introduced later.

By replacing La of $LaO_{1-x}F_xBiS_2$ by other RE, various BiS_2-based superconductors were developed: $CeO_{1-x}F_xBiS_2$, $PrO_{1-x}F_xBiS_2$, $NdO_{1-x}F_xBiS_2$, $BiO_{1-x}F_xBiS_2$, and RE-site solution phases [3,10–17]. Furthermore, carrier doping by partial substitution of M^{4+} (M: Ti, Zr, Hf, Th) for the La^{3+} site was reported [18]. Among them, the phases with RE = La and Ce do not show bulk superconductivity, but the phases with RE = Pr, Nd, and Bi exhibit bulk superconductivity with a large shielding fraction in the susceptibility data. At ambient pressure, all the phases crystalize in the same tetragonal structure (*P*4/*nmm*). The difference is understood by the difference in in-plane CP.

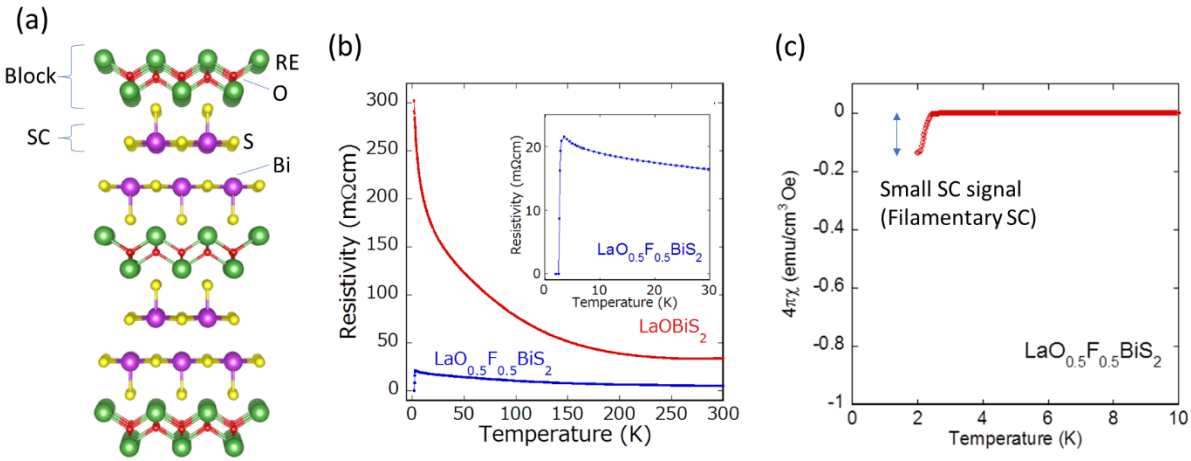

Figure 2. (a) Crystal structure image of $LaO_{0.5}F_{0.5}BiS_2$. (b,c) Temperature dependences of (b) electrical resistivity and (c) magnetic susceptibility of $LaOBiS_2$ and $LaO_{0.5}F_{0.5}BiS_2$. Partly reproduced from Ref. 2.

For RE = La and Ce, however, application of external pressure effects including high-pressure annealing induces bulk superconductivity [2,19–22], which is accompanied with structural distortion into monoclinic structure ($P2_1/m$, No. 11) [23]. In addition, the phases with RE = Pr and Nd also exhibit a slight increase in T_c under high pressure [24]. From these results,

it is clear that there is a correlation between the superconducting properties and the crystal structure in BiS_2-based superconductors.

1.2 In-plane chemical pressure

Chemical pressure effect is used to modify physical properties of materials, where the unit-cell volume or specific chemical bonds are expanded or compressed by chemical substitution. To generate effects similar to physical pressure effects, isovalent substitutions are normally used to control the crystal structure without large change in electronic structure.

In BiS_2-based superconductors, two methods of applying CP are developed in the case of $LaO_{0.5}F_{0.5}BiS_2$ [9,14,24]. One of the methods is substitution of La^{3+} (116 pm: Shannon's radius) by smaller RE^{3+} ions like Ce^{3+} (114 pm), Pr^{3+} (113 pm), Nd^{3+} (112 pm), or Sm^{3+} (108 pm) [Fig. 3(a)]. As shown in the superconductivity phase diagram [Fig. 3(c)], filamentary superconductivity observed for RE = La is suppressed by partial substitution of Ce, and at RE = $Ce_{0.6}Nd_{0.4}$, bulk superconductivity appears in $REO_{0.5}F_{0.5}BiS_2$ [14]. Furthermore, the localized behavior in resistivity is suppressed by the smaller-RE substitution [3].

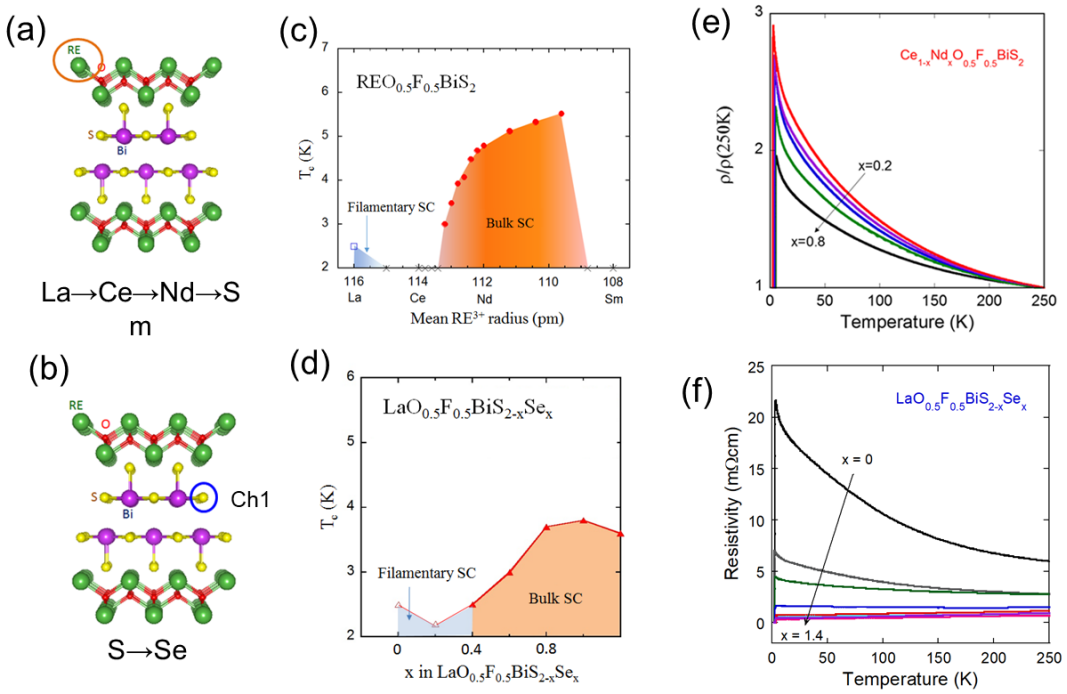

Figure 3. (a,b) Schematic images of crystal structure for (a) RE-substituted and (b) Se-substituted (at Ch1) phases of $REO_{0.5}F_{0.5}BiCh_2$. (c,d) Superconductivity phase diagram for (c) $REO_{0.5}F_{0.5}BiS_2$ and (d) $LaO_{0.5}F_{0.5}BiS_{2-x}Se_x$. (e,f) Temperature dependences of electrical resistivity for (e) $REO_{0.5}F_{0.5}BiS_2$ (normalized for comparison) and (f) $LaO_{0.5}F_{0.5}BiS_{2-x}Se_x$. Partly reproduced from Ref. 3.

Similar trends were observed in Se-substituted $LaO_{0.5}F_{0.5}BiS_{2-x}Se_x$ [Fig. 3(b)]; smaller S^{2-} (186 pm) is substituted by larger Se^{2-} (198 pm) [24]. With increasing Se concentration, bulk superconductivity is induced [Fig. 3(d)], and metallicity is enhanced by Se substitution [Fig. 3(f)]. The similar phase diagrams between $REO_{0.5}F_{0.5}BiS_2$ [Fig. 3(c)] and $LaO_{0.5}F_{0.5}BiS_{2-x}Se_x$ [Fig. 3(d)] cannot be understood by the unit-cell CP effects. The RE substitution with smaller RE results in compression of the volume, but Se substitution for the S site results in expansion of the volume because Se^{2-} is larger than S^{2-}. Therefore, the changes in lattice constants *a* and *c* upon the substitution also exhibit different trends. Schematic images on the evolutions of lattice constants, particularly in-plane (*a*-axis), are summarized in Fig. 4(a). To understand the commonality in these two substitution effects, which exhibit similar superconductivity phase diagrams, the estimation of ***in-plane chemical pressure*** on the in-plane Bi-Ch1 bond was proposed [9]. The in-plane CP is defined with ionic radius including $Bi^{2.5+}$ radius estimated from single-crystal structural analysis of $LaO_{0.54}F_{0.46}BiS_2$.

$$\text{In-plane CP} = [R_{Bi} + R_{Ch1}] / [\text{Bi-Ch1 distance (in-plane)}] \qquad (1\text{-}1)$$

Here, R_{Bi} is the ionic radius of $Bi^{2.5+}$, and R_{Ch1} is average ionic radius at the Ch1 site. Bi-Ch1 distance (in-plane) can be estimated from X-ray diffraction and Rietveld refinement (see Appendix for Rietveld refinement).

As shown in Fig. 4(d), the *x* (RE or Se substitution) dependences of in-plane **CP** estimated using equation (1-1) exhibit a positive increase on substitution for both systems. Figure 4(b) shows the schematic image of the concept of in-plane **CP** in $REO_{0.5}F_{0.5}BiS_2$ and $LaO_{0.5}F_{0.5}BiS_{2-x}Se_x$. This situation can be understood by considering the differences in bonding stiffness in the in-plane Bi-S bonds and others. X-ray absorption spectroscopy studies revealed the difference in bond stiffness by analyzing the temperature dependence of Debye-Waller factor; the similar trend was observed in various $BiCh_2$-based systems [25,26]. Basically, in-plane Bi-Ch1 has flexible bonding nature and others, particularly blocking layer with ionic bonds, possess stiff bonding nature. When smaller RE is substituted, the blocking layer is compressed, which is smoothly linked to the compression of Bi-Ch1 plane. In the case of Se substitution, the constituent elements of the LaO layer are not changed by the Se substitution, and Se is selectively substituted at the in-plane site [27]. The substitution of Se for the in-plane

S site results in the in-plane expansion, but the expansion is suppressed by the stiff blocking layer structure. Finally, the direction of in-plane CP for these two systems becomes the same.

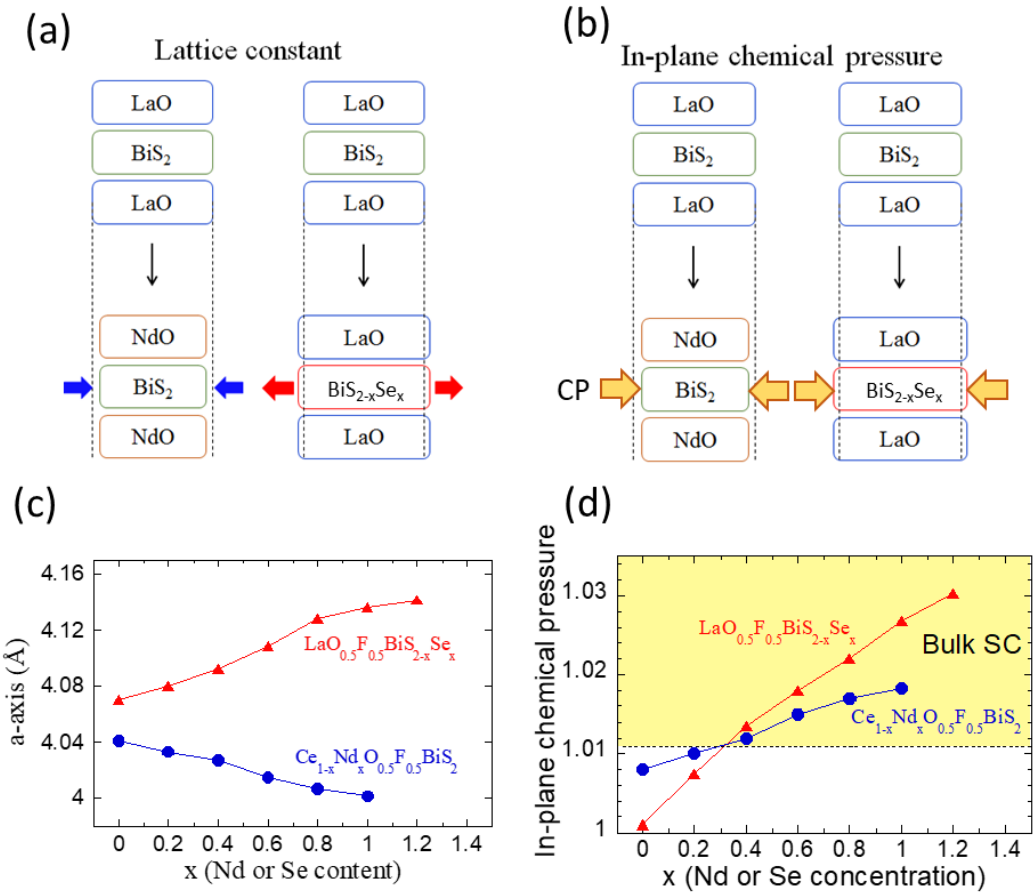

Figure 4. (a,b) Schematic images of the change in (a) lattice constant and (b) in-plane CP. Blue and red arrows indicate compression and expansion of lattice constant, respectively. (c,d) *x* (substitution) dependences of (c) lattice constant *a* and (d) in-plane CP.

1.3 In-plane disorder in $BiCh_2$-based layered system

As mentioned above, $LaO_{0.5}F_{0.5}BiS_2$ is a filamentary superconductor, and the phenomenon was thought to be caused by the weak carrier localization. The in-plane CP was effective to suppress the carrier localization and induce bulk superconductivity. This in-plane CP effect on the carrier localization is explained by the suppression of in-plane static disorder revealed in synchrotron X-ray diffraction, neutron diffraction, and X-ray absorption spectroscopy [28–33]. From Rietveld refinement of synchrotron X-ray diffraction data for the Se-substituted system with anisotropic analysis of atomic displacement parameter with U_{11}

(in-plane) and U_{33} (out-of-plane) [Fig. 5(b)] [28], it was found that U_{11} for the Ch1 site is quite large for the phase with low in-plane CP.

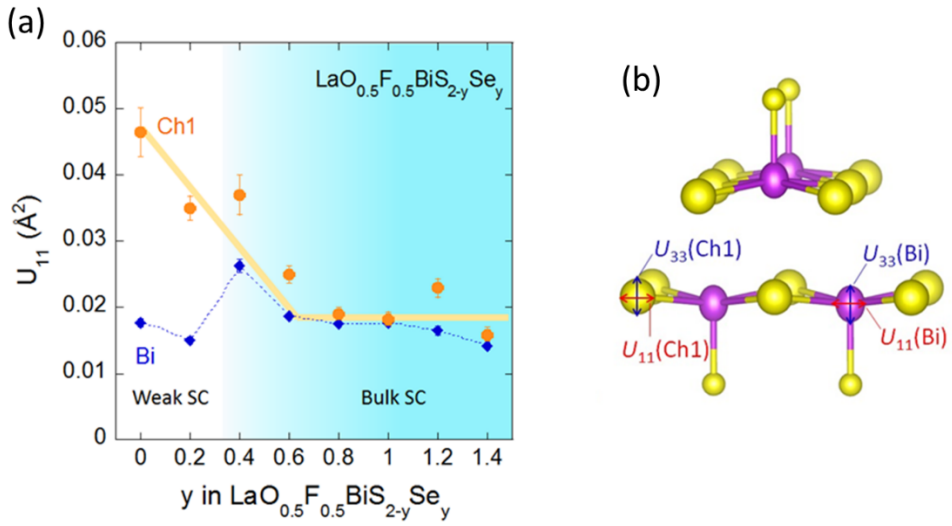

Figure 5. (a) Se substitution dependence of in-plane displacement parameter U_{11} for $LaO_{0.5}F_{0.5}BiS_{2-y}Se_y$. (b) Schematic images of U_{11} (in-plane) and U_{33} (out-of-plane) displacement parameters depicted with thermal ellipsoids on the $BiCh_2$ layers. Reproduced from Ref. 3.

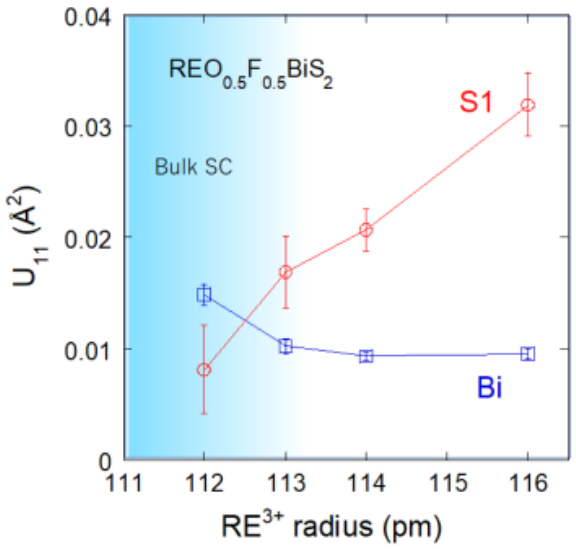

Figure 6. RE ionic radius dependence of U_{11} for Bi and S1 sites for $REO_{0.5}F_{0.5}BiS_2$. Reproduced from Ref. 3.

With increasing in-plane CP, U_{11} decreases and becomes comparable as U_{11} for Bi as shown in Fig. 5(a). In the regime, bulk superconductivity is induced. The results are consistent with the extended X-ray absorption fine structure (EXAFS): amorphous-like Bi-Ch1 bond nature

in a phase with low CP and evolution of crystal-like Bi-Ch1 bond nature by in-plane CP [32]. Similar trend was observed in RE-substituted system; U_{11} for in-plane S1 is suppressed by smaller-RE substitution as show in Fig. 6 [29]. As shown in Fig. 7, both RE-substituted and Se-substituted systems exhibit the suppression of U_{11} for the Ch1 site and bulk superconductivity. Therefore, to induce bulk superconductivity in $REOBiS_2$-based compounds, both electron carrier doping and the suppression of in-plane U_{11} are needed. From the temperature dependence of displacement parameters, the large displacement at the in-plane Ch1 site was found to be static local distortion.

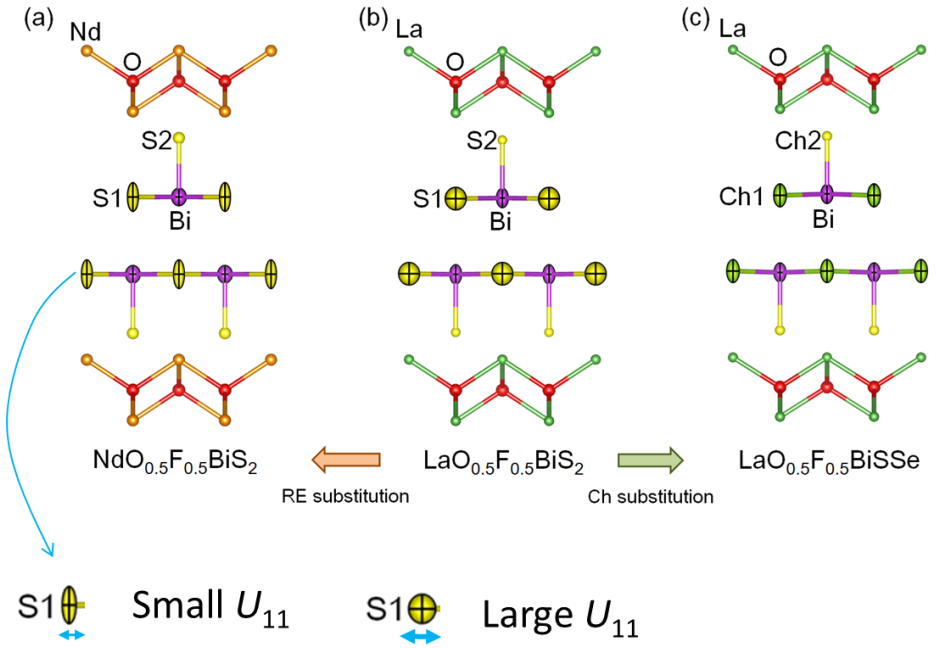

Figure 7. Schematic images of crystal structure with thermal ellipsoids of U_{11} and U_{33} for (a) $NdO_{0.5}F_{0.5}BiS_2$ with high CP, (b) $LaO_{0.5}F_{0.5}BiS_2$ with low CP, and (c) $LaO_{0.5}F_{0.5}BiSSe$ with high CP. Partly reproduced from Ref. 3.

Since these facts are related to our conclusion of this study, we describe our assumption on the relationship between the local in-plane disorder and the appearance of Bi vibration along the *c*-axis. In the following subsections, we show that the $BiCh_2$-based compounds have low-energy optical phonon modes that are mainly related to the Bi vibration along the *c*-axis. When in-plane CP is weak (namely $LaOBiS_2$), the local in-plane disorder is huge, and the system has glassy in-plane structure; namely there are randomly distributed local distortions [30-33]. This

would cause the suppression of expected Bi vibration along the *c*-axis, and that was actually observed in this study.

1.4 Phonon instability and charge density wave

Soon after the discovery of the BiS_2-based superconductors, phonon calculation was performed, and the presence of phonon instability was proposed [34,35]. The theoretical analyses proposed the presence of anharmonic ferroelectric soft phonons and possible charge density wave (CDW) transition in the BiS_2-based materials. Yildirim proposed in-plane distortion with a large displacement of S in $LaOBiS_2$, which is consistent with experimentally observed in-plane displacements of in-plane Ch. Furthermore, a CDW transition was experimentally observed in $LaO_{1-x}F_xBiS_2$ and $EuFBiS_2$ [36,37]. For both materials, possible CDW formation was observed at temperatures just below room temperature. The in-plane Ch1 disorder should be linked to the formation of CDW states. In addition, the anharmonic nature of phonons would be linked to physical properties of $BiCh_2$-based compounds. This fact motivated us to study the in-plane CP effects on lattice anharmonicity in the system.

After phonon calculation, inelastic neutron scattering (INS) was performed for $LaO_{1-x}F_xBiS_2$ ($x = 0$ and 0.5) [38]. For both $x = 0$ and 0.5, low-energy phonons are almost unchanged, but high-energy phonons are modified by F substitution. The low-energy phonons are mainly dominated by the contribution of the Bi, and the low-energy mode with a large density of states (DOS) corresponds to Bi vibration along the *c*-axis.

1.5 Thermoelectric properties in $LaOBiS_{2-x}Se_x$

The $LaOBiS_{2-x}Se_x$ phases exhibits a high thermoelectric performance. As described in Appendix, the thermoelectric dimensionless figure-of-merit ZT is defined as $ZT = S^2T/\kappa\rho$ where S, T, κ, and ρ are Seebeck coefficient, absolute temperature, thermal conductivity, and electrical resistivity, respectively. In addition, power factor, which is a part of ZT, is defined as $PF = S^2/\rho$. In $LaO_{1-x}F_xBiS_2$, F substitution results in a decrease in PF due to excess carriers, which decreases absolute S [39]. However, Se substitution in $LaOBiS_{2-x}Se_x$ largely improves the PF owing to the increase in carrier mobility [40], and high ZT of 0.36 was achieved [41,42]. The improvement of mobility can be explained by the in-plane CP effects, which result in the suppression of in-plane Bi-S bond disorder, which was revealed by EXAFS [33].

However, the suppression of in-plane Bi-S bond disorder cannot explain the decrease in lattice thermal conductivity by Se substitution [42]; in x = 1.0 (LaOBiSSe), the Bi-Ch in-plane has a less disordered structure and less S/Se randomness because of selective occupation of Se at the in-plane site [43]. To answer this issue, the importance of lattice anharmonicity to low lattice thermal conductivity, which enhances ZT, in a thermoelectric phase of BiS_2-layered $LaOBiS_{2-x}Se_x$ has recently been proposed [44]. INS measurements revealed that the low-energy optical phonon mode exhibits softening with increasing Se concentration in the $LaOBiS_{2-x}Se_x$, and that is linked to the suppression of lattice thermal conductivity. The optical phonons with E = 6-7 meV in the $LaOBiCh_2$-type materials correspond to Bi vibrations, and the major phonon density of states (DOS) are of c-axis vibration of Bi [44]. Figure 8 shows the calculated phonon DOS for $LaOBiS_2$. It is clear that the low-energy phonon modes are dominated by the Bi vibrations. The largest DOS peak at the low-energy regime is A_1 mode that corresponds to Bi vibration along the c-axis [38,44]. The presence of large-amplitude vibration of Bi along the c-axis was also seen via U_{33} of Bi in LaOBiSSe [43]. The temperature dependence of U_{33} with a large residual U_{33} at T = 0 K is consistent with the possibility of anharmonic c-axis vibration of Bi.

The trends on low-energy phonons are common between non-doped $LaOBiS_2$ and doped (superconducting) $LaO_{0.5}F_{0.5}BiS_2$ [38]. Therefore, we consider that the detailed investigation on the low-energy phonons will provide us with useful information to understand superconductivity mechanisms in the $BiCh_2$-based family as well as thermoelectric phases.

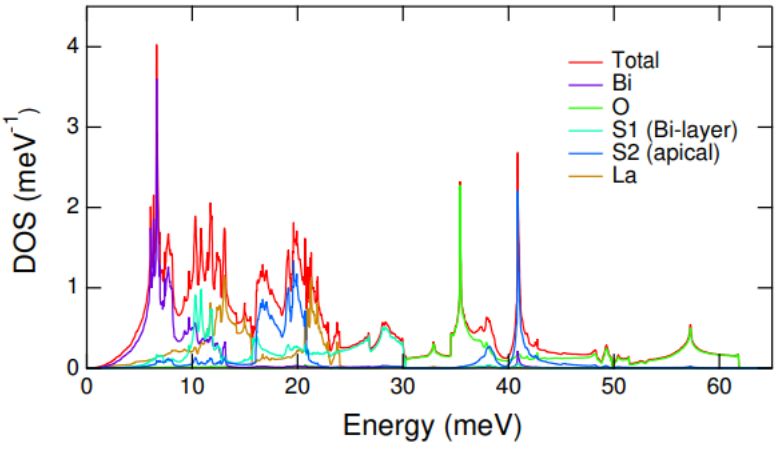

Figure 8. Calculated phonon DOS for $LaOBiS_2$. In the calculation, monoclinic structure was used to stabilize the crystal structure. However, the trends should be applicable to the tetragonal structure [44].

2. Purpose of this study

$BiCh_2$-based layered compounds exhibit superconductivity in the electron-doped phases and high thermoelectric performance in the non-electron-doped phases. To induce bulk superconductivity, both carrier doping and in-plane CP on in-plane Bi-Ch bond are needed. For example, Se substituted $LaO_{0.5}F_{0.5}BiS_{2-x}Se_x$ exhibits bulk superconductivity with Se substitution. The in-plane CP suppresses local in-plane distortion, which is the cause of the weak carrier localization in samples with less in-plane CP. To enhance thermoelectric performance, in-plane CP for a non-doped system is useful because the in-plane CP improves power factor *PF* through the improvement of carrier mobility. For example, Se substitution in $LaOBiS_{2-x}Se_x$ improves the power factor. In addition, the in-plane CP affects Bi large-amplitude vibration along the *c*-axis. From inelastic neutron scattering, the phonon energy softening was observed for Se-substituted $LaOBiS_{2-x}Se_x$. The softening is linked to the suppression of lattice thermal conductivity, and hence, thermoelectric dimensionless figure-of-merit *ZT* is improved by both the increase in *PF* and the decrease in κ.

As described in the introduction part, in-plane CP (typically achieved by Se substitution in the conduction Bi-Ch plane) is essential for both the emergence of bulk superconductivity and high thermoelectric *ZT*. Although studies on the effect of in-plane CP on the in-plane local distortion (Bi-Ch bond disorder) have been performed by several probes (synchrotron X-ray diffraction, neutron scattering, EXAFS), the investigation on the in-plane CP on the *c*-axis Bi vibration has been done by the inelastic neutron scattering only. Hence, the correlation between the *c*-axis Bi vibration and physical properties in $BiCh_2$-based systems were unclear.

The main purpose of this study is to clarify the effects of in-plane CP on the *c*-axis Bi vibration in $BiCh_2$-based compounds including carrier-doped superconducting compositions, $LaO_{0.5}F_{0.5}BiS_2$ and $LaO_{0.5}F_{0.5}BiSSe$, and non-doped thermoelectric compositions, $LaOBiS_2$ and LaOBiSSe. On the basis of previous studies on displacement parameter, inelastic neutron scattering, and phonon calculations, we assumed that the *c*-axis Bi vibration enhances anharmonicity. Therefore, our purpose of this study is to clarify how the c-axis vibration is affected by the in-plane CP and how the anharmonicity is changed.

3. Methods

3.1 Synthesis of samples

In this work, polycrystalline samples of RE(O,F)$BiS_{2-x}Se_x$ were synthesized by a solid-state-reaction method, and the obtained samples were densified by high-pressure (HP) annealing. Here, we briefly describe the methods of synthesis. Information of the powders or grains used for the syntheses will be described in the end of subsection. The starting materials were mixed with a nominal composition of the target phase in a mortar, and pelletized into a pellet. The pellet was sealed in an evacuated quartz tube, and heated at the optimal conditions. In most cases, the sintering temperature was 700°C, and the heating duration was 15–20 h. The obtained sample was ground, pelletized, and annealed in the same procedure as the first sintering.

To obtain dense samples for sound velocity measurements, we performed HP annealing in a cubic-anvil-type 180-ton press. A sample pellet with a diameter of 5 mm was placed in a BN crucible, which is set in a carbon heater capsule. The carbon heater was set in a pyrophyllite block, and the cube was placed in the high-pressure synthesis machine. With six anvils, isotropic pressure was applied, and the sample temperature was increased by applying current to the carbon capsule. Here, we applied 1.5 GPa and heated the sample at 400°C for 10–15 minutes. With this HP annealing conditions, crystal structural modification is less, but a high relative density to ideal value greater than 90% can be achieved.

For example, polycrystalline samples of $LaOBiS_{2-x}Se_x$ ($x = 0, 0.5, 1.0$) were synthesized by a solid-state reaction method. We began with powders of La_2S_3 (99.9%), La_2O_3 (99.9%), S (99.99%), Se (99.99%), andBi_2S_3 (made from Bi and S), Bi_2Se_3 (made from Bi and Se) and grains of Bi (99.999%) as the starting materials. Powders of Bi_2S_3 and Bi_2Se_3 were made through a reaction that took place in an evacuated quartz tube. The heating treatment was conducted for15 hours at 700° C. For F-substituted samples, REF_3 (99.9%) powders are additionally used.

3.2 Crystal structure analysis and phase characterization

The crystal structure of a material determines its physical characteristics. Crystal structure analysis is therefore a crucial component of this study. Particularly, in this study,

volumetric thermal expansion of lattice constant is an essential parameter in the estimation of Grüneisen parameter. We used X-ray diffraction (laboratory X-ray source and synchrotron X-ray) to analyze crystal structure of the synthesized samples. To characterize the actual composition of the obtained samples, SEM-EDX was used.

3.2.1 X-ray diffraction (laboratory XRD)

To determine phase purity and crystal structure, powder X-ray diffraction (XRD) was performed on a diffractometer Miniflex-600. We collected the XRD pattern at $2\theta = 10^{\circ}$ to 70° using the traditional θ - 2θ method. This is outfitted with a high-speed silicon strip D/teX-Ultra detector and CuKα radiation (λ = 1.5418 Å). The obtained data were analyzed by Rietveld method [45] using RIETAN-FP program [46]. The detailed explanation of Rietveld refinement is written in Appendix. To estimate temperature dependence of lattice constants, we performed high-temperature XRD on Miniflex-600 using a high-temperature stage BTS-500 in vacuum. To visualize the refined crystal structure images, we used VESTA software [47].

3.2.2 Synchrotron X-ray diffraction

We also used synchrotron X-ray diffraction (SXRD). Because of its variable wavelength, high flux, and superior collimator for the incident beam of synchrotron radiation, SXRD, in contrast to conventional laboratory XRD, exhibits improved resolution and sensitivity of XRD peaks to determine the crystalline size, sensitivity, and atomic coordinates with atomic displacements in crystal. In addition, the short measurement time enables us to perform temperature-variable XRD experiments easily. Figure 9 depicts a condensed schematic of the synchrotron X-ray generated in the storage ring at the synchrotron facility.

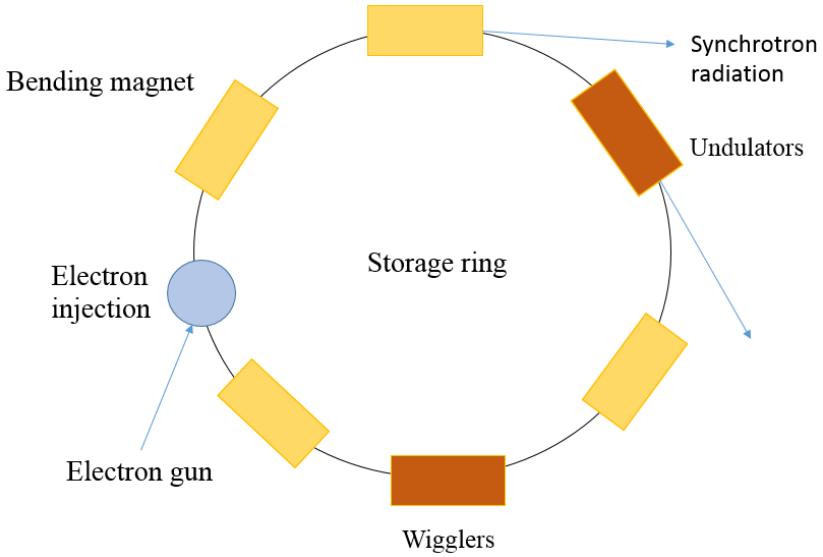

Figure 9. Schematic diagram of a synchrotron storage ring.

We used beamline BL02B2 of SPring-8 for low- and high-temperature SXRD experiments. The diffraction data was collected using multiple-MYTHEN detector [48]. The samples were sealed in an evacuated quartz capillary, and the temperature of the sample was controlled by N_2 gas. Typical X-ray energy was 25 keV, and the actual value of wave length was determined from the lattice constant of CeO_2. The obtained data were analyzed by Rietveld method using the RIETAN-FP program.

3.2.3 Scanning electron microscopy (SEM)

We observed the surface of the obtained samples by scanning electron microscope TM-3030 (Hitachi-hightech). Here, we briefly describe the mechanism of SEM observation. With high resolution and magnification, SEM offers an image of the sample materials. From the electron gun, a highly focused and intense electron was fired, which then struck the specimen sample in a raster scan pattern. The electrons in the sample and the electrons in the beam interact differently. The two basic types of dispersion are the elastic scattering and the inelastic scattering. When the incident electron collides with the samples without losing any energy, elastic scattering takes place. he electron gun's electron direction has been altered. Backscattered electrons are what we name this electron (BSE). An inelastic electron, on the

other hand, is a form of electron where the electron loses energy following an incident. Secondary electrons are referred to as dispersed electrons, whereas incident electrons are known as main electrons. These second-order electrons are found at the detector located outside the object, and in the SEM, they are employed to create an image signal. These indications include heat, secondary electrons, recognizable X-rays, and backscattered electrons (BSE). The secondary and BSE electrons, as well as their combined version, are used to create the SEM image. An example of the SEM image of our sample is shown in Fig. 10.

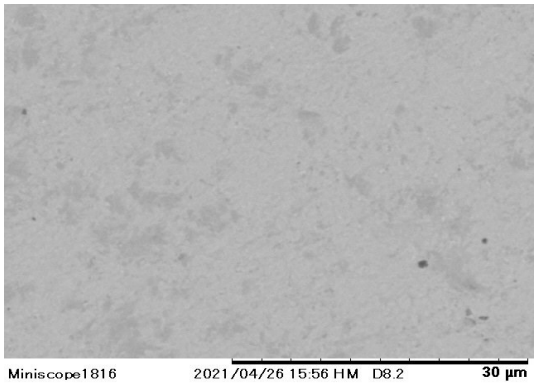

Figure 10. SEM image for $LaOBiS_{2-x}Se_x$ taken using backscattered electrons.

3.2.4 Energy dispersive X-ray (EDX) analysis

The actual composition of the obtained samples was investigated by energy dispersive X-ray spectroscopy (EDX) on the SEM (TM-3030, Hitachi-high tech) equipped with an EDX analyzer SwiftED (Oxford). Here, we briefly explain the mechanism of the EDX experiment. When an electron beam with appropriate energy strikes an electron in the inner cell of the sample with lower energy, the electron is ejected from the shell and causes an X-ray emission. The vacancy was then filled by a high-energy electron from the outer cell, which releases X-ray radiation, characteristic X-ray as explained in Fig. 11, that is specific to each element. By analyzing an energy spectrum, an energy-dispersive X-ray (EDX) is performed to identify various components. The individual elements of the sample are easily identified because the energy spectra of each element are distinct. The associated computer is used to control the EDX system. SEM equipment is frequently included with EDX apparatus. Compositional analysis data is produced for a wide range of elements and compounds using the combination of those two. Spot size or an area of an SEM image in the order of micrometers is selected to study the sample.

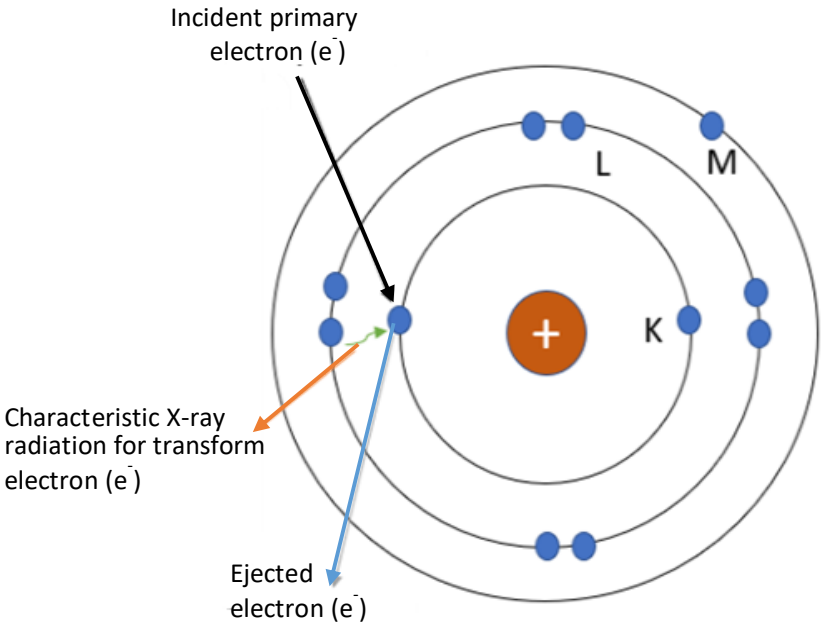

Figure 11. Schematic image of the emergence of characteristic X-ray radiation.

3.3 Physical properties measurements

We measured magnetization, specific heat, and sound velocity of the obtained samples. Here, we briefly explain the methods used for those experiments.

3.3.1 Magnetization

We used Magnetic Property Measurement Systems MPMS3 (Quantum Design), which is equipped with a superconducting quantum interference device (SQUID) magnetometer (dc-SQUID). The magnetization measurements were performed after both zero-field cooling (ZFC) and field cooling (FC) with a typical applied field of 10 Oe. SQUID-VSM mode was used for collecting the temperature dependence data. Sample was packed in nonmagnetic capsule and placed in a brass sample holder for VSM mode.

3.3.2 Specific heat

The specific heat measurements were performed to investigate the superconducting properties, Debye temperature, and phonons. We used Physical Property Measurement System PPMS (Quantum Design) to take specific heat data with relaxation method. The sample was

placed on the sample stage using Apiezon N grease. We briefly explain the sample stage (Fig. 12) of the specific heat measurement. There is a heat controller that adds heat to a sample and thermometer.. As a result, specific heat of the sample is determined by the temperature change to the provided heat after subtracting addenda specific heat. Before sample measurements, we measured addenda specific heat.

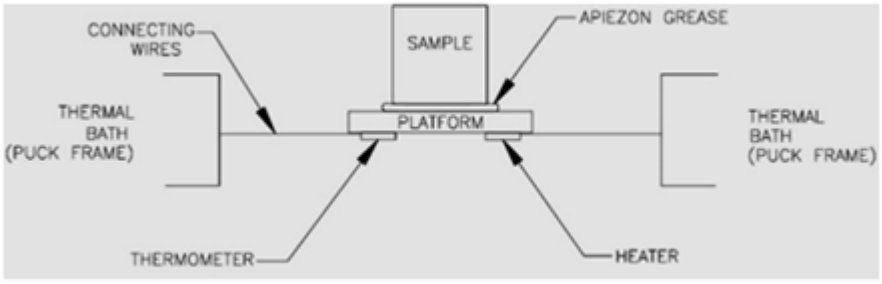

Figure 12. A schematic diagram of specific heat sample stage.

3.3.3 Sound velocity

We measured longitudinal sound velocity (v_L) of the densified samples at room temperature using ultra-sonic thickness detector (Satotech-2000C). Since high packing density results in reliable estimation of v_L, we measured HP annealed samples with a relative packing density greater than 95 %. The sample was attached with Kaplant gels to the detector during the measurements.

4. Investigation of phonon by specific heat

To clarify the in-plane CP effects on phonons, particularly the Bi large-amplitude vibration long the *c*-axis, we analyzed lattice specific heat (C_{lat}) in a C_{lat}/T_3 form. The analyses are based on previous works on low-energy optical phonons. In this chapter, we start with the introduction of the previous works and the analysis procedures.

4.1 Introduction

The specific heat of inorganic solids is mainly contributed by lattice (C_{lat}), electron (C_{el}), and magnetism (spin), and C_{lat} is well explained by the Debye model (C_D) [equation (4-1)].

$$C_D = 9Nk_B\left(\frac{T}{\theta_D}\right)^3 \int_0^{x_D} dx \frac{x^4 e^x}{(e^x-1)^2} \qquad (4\text{-}1)$$

where N, k_B, and θ_D, are the number of atoms, Boltzmann constant, and Debye temperature, respectively, and x_D is equal to θ_D/T. The target physical parameter of this study is C_{lat}, and the specific heat of the $BiCh_2$-based compounds can be regarded as C_{lat} and C_{el}. For C_{el}, low-temperature approximation gives $C_{el} = \gamma T$ where γ is electronic specific heat coefficient.

The analysis of optical phonons has been performed on materials with a caged structure, rattling motion of atoms, flexible network or anomalous thermal expansion [49–54]. The simplest analysis is the inclusion of one Einstein model (C_E) with C_D. The C_E is described as follows with Einstein temperature (θ_E). If there are large optical phonon contributions with a low θ_E, a hump structure is observed in the temperature dependence of C_{lat}/T^3.

$$C_E = 3Nk_B\left(\frac{\theta_E}{T}\right)^2 \frac{\exp\left(\frac{\theta_E}{T}\right)}{\left[\exp\left(\frac{\theta_E}{T}\right)-1\right]^2} \qquad (4\text{-}2)$$

For the analysis of the temperature dependence of C_{lat}, the summation of equation (4-3) is usually assumed using oscillator number strength (n_i). When assuming single atom in the formula unit, the summation of n_i should be 1, and it is multiplied by the number of atoms in the unit cell according to the unit of specific heat.

$$C_{lat} = \sum_{i,j} n_{Di} C_{Di} + n_{Ej} C_{Ej} \qquad (4\text{-}3)$$

In the case of complicated structure or atomic vibration characteristics, summation of multiple Debye and Einstein models were used to explain C_{lat} [52–54]. The well-known example is the specific heat analysis on negative thermal expansion material ZrW_2O_8 [53]. The use of multiple Debye models results in multiple θ_Ds, and the concept is well described in Refs. 55 and 56. When the atomic numbers of the constituent elements are largely different, or atomic vibration

characteristics are different on each atom or component molecules, multiple θ_Ds are assumed in the analysis. For example, when assuming three θ_Ds, the average θ_D is described as equation (4-4) using oscillator number strength n_{Di} and Debye temperature θ_{Di} [55].

$$\frac{n_{D1}+n_2+n_3}{[\theta_D(\text{average})]^3} = \frac{n_{D1}}{\theta_{D1}^3} + \frac{n_{D2}}{\theta_{D2}^3} + \frac{n_{D3}}{\theta_{D3}^3} \qquad (4\text{-}4)$$

In this study, we investigated phonons by analyzing C_{lat} for $BiCh_2$-based compounds $LaOBiS_{2-x}Se_x$ and $LaO_{0.5}F_{0.5}BiS_{2-x}Se_x$ to investigate the effects of in-plane CP on the optical phonons. As a result, we needed to use two Debye models to extract the contributions of optical phonon modes. We assumed two cases (case 1 and 2) to fix n_{D1} and n_{D2} for all the samples. Case 1 assumes $n_{D1} : n_{D2} = 2 : 3$ where we consider that Bi and Ch1 in the flexible conducting plane have a lower θ_D, and other three atoms have a higher θ_D [57]. For the analysis of specific heat, we used the unit of J/K mol(f.u.) where five atoms are included in a formula unit (f.u.) of $LaOBiS_2$. This assumption is based on the observation of low stiffness in the Bi-Ch1 in-plane bonds by EXAFS [26]. Case 2 assumes $n_{D1} : n_{D2} = 10/3 : 5/3$ where we assume the difference of transverse and longitudinal sound velocities. For both cases, Einstein components (oscillator number strength) are compensated by reducing n_{D1} for a lower θ_D.

4.2 $LaOBiS_{2-x}Se_x$

For specific heat measurement, we measured the T dependence of C for the polycrystalline samples of $LaOBiS_{2-x}Se_x$ (x = 0, 1.0) at T = 1.9–300 K [57]. For $LaOBiS_{2-x}Se_x$, data taken at H = 0 T were used for the analyses because there is no superconducting transition.

In $LaOBiS_2$, the total C is contributed by C_{lat} only because of no carrier doping. Figure 13(a) shows the C-T data for $LaOBiS_2$, and Fig. 13 (b) shows the fitting to $C/T = \beta T^2$ where β is the coefficient of lattice specific heat. From the obtained β, θ_D is estimated as 222.6(4) K. First, analysis with a single Debye model (model 1) was tested, and the result is shown in Fig. 13(c). Because of assumed atomic number of 5 per formula unit, the sum of n should be 5 in the analyses. clear that a single Deby model with θ_D = 223 K does not explain the experimental data. We tested a single Debye model with different θ_D, but no successful fitting was obtained. Therefore, we analyzed the specific heat data with case 1 and 2. For case 1, we could use θ_D = 222.6(4) K estimated from low-T data for one of the θ_Ds. However, for case 2, both θ_Ds should be higher than 222.6(4) K.

Case 1

The analysis results for $LaOBiS_2$ in case 1 are summarized in Figs. 13(d–f) and Table I. Model 2 uses two Debye models (model 2), and model 3 and 4 uses additional single and triple Einstein models as shown in Figs. 13(d–f).

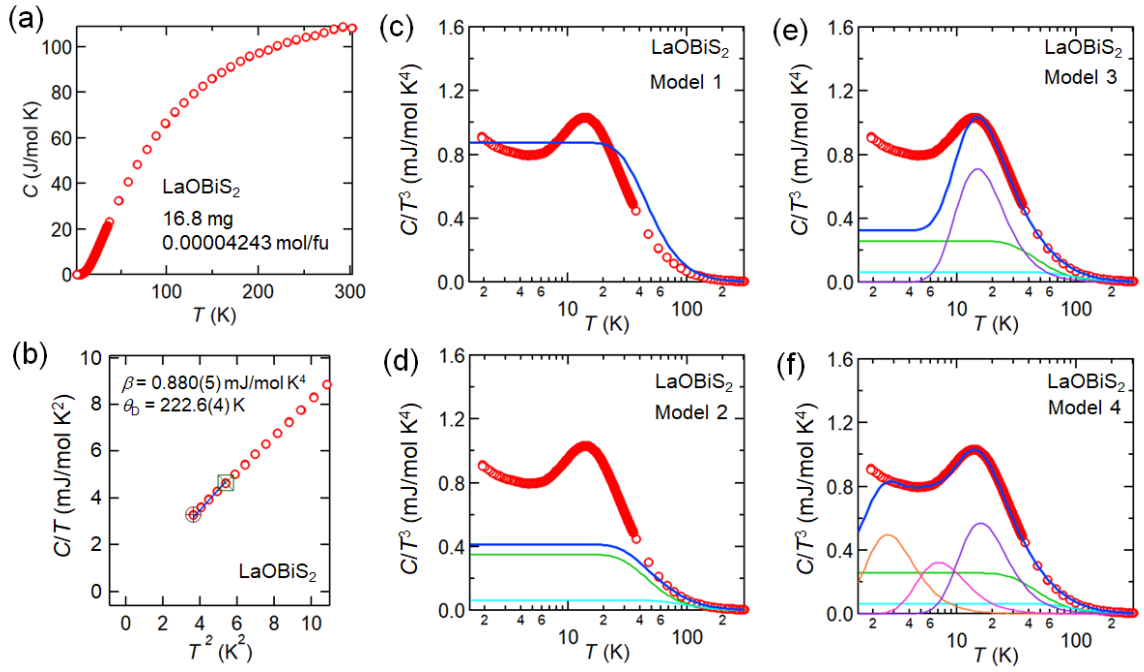

Figure 13. (a) Temperature dependence of specific heat (C) for $LaOBiS_2$. (b) Low-T fitting result on the T^2 dependence of C/T, where data points between two cursors were used for fitting. (c-f) Analyses of C/T^3 with different four models: model 1 with single Debye model, model 2 with double Debye models, model 3 with double Debye and single Einstein models, and model 4 with double Debye and triple Einstein models. The horizontal axis is in log scale. Reproduced from Ref. 57.

Table I. The parameters used for the C/T^3 analyses for $LaOBiS_2$ [57] in case 1.

Model parameter	Model 1	Model 2	Model 3	Model 4
θ_{D1} (n_{D1})	223 K (n = 5)	223 K (n = 2)	223 K (n = 1.48)	223 K (n = 1.46195)
θ_{D2} (n_{D2})		450 K (n = 3)	450 K (n = 3)	450 K (n = 3)
θ_{E1} (n_{E1})			73 K (n = 0.52)	78 K (n = 0.51)
θ_{E2} (n_{E2})				35 K (n = 0.026)
θ_{E3} (n_{E3})				13 K (n = 0.00205)

We applied double Debye models, and the combination of θ_{D1} = 223 K (n_{D1} = 2) and θ_{D2} = 450 K (n_{D2} = 3) gave a good fitting at a high-temperature data as shown in Fig. 13(d) where n_{D1} and n_{D2} are corresponding oscillator numbers. From the results, we fix θ_{D1} (lower θ_D) to be the value obtained by low-T fitting to the C/T-T^2 plot. In addition, n_{D2} is fixed to 3, which is reasonable when considering that La and O in blocking layers and S2 are contributing a higher θ_{D2}, and lower θ_{D1} is contributed by Bi and S1 in the conducting plane with anomalous bonding states with local disorder and Bi vibration along the c-axis. Basically, C with a lower θ_D dominates low-T C_{lat}, which is the reason why θ_{D1} estimated from the fitting in Fig. 13(b) could work as θ_{D1}. In Fig. 13(e), one Einstein mode with θ_{E1} is added to the model in Fig. 13(d). To create n_{E1}, n_{D1} was reduced accordingly, because the low-energy phonons are mainly contributed by Bi as discussed later. Finally, as shown in Fig. 13(f), a model with double Debye and triple Einstein modes was found to well explain the experimental result. Although residual C/T^3 is present at lower temperatures, we did not include further Einstein modes because the expected peak positions are lower than the lowest data point, and the oscillator number of that mode is extremely low. The obtained model parameters for $LaOBiS_2$ are summarized in Table I. Although we used three Einstein modes for fitting, the Einstein model with the highest θ_{E1} has a large n, which implies the presence of major vibrations of Bi at the energy of θ_E = 78 K.

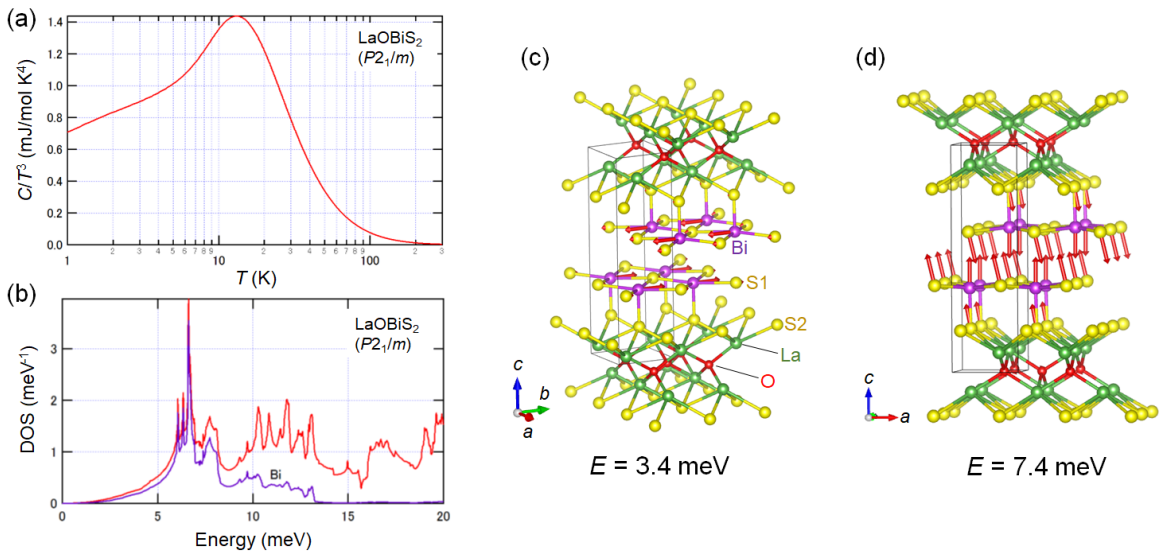

Figure 14. (a) Calculated temperature dependence of C/T^3 for $LaOBiS_2$ with a monoclinic $P2_1/m$ structure. The horizontal axis is in log scale. (b) Energy dependence of phonon DOS for $LaOBiS_2$. The original data has been published in Ref. 44, and the simplified version is shown here. (c,d) Schematic images of crystal structure of $LaOBiS_2$ and atomic vibrations at E = 3.4 and 7.4 meV. The arrows indicate displacements of the atoms.

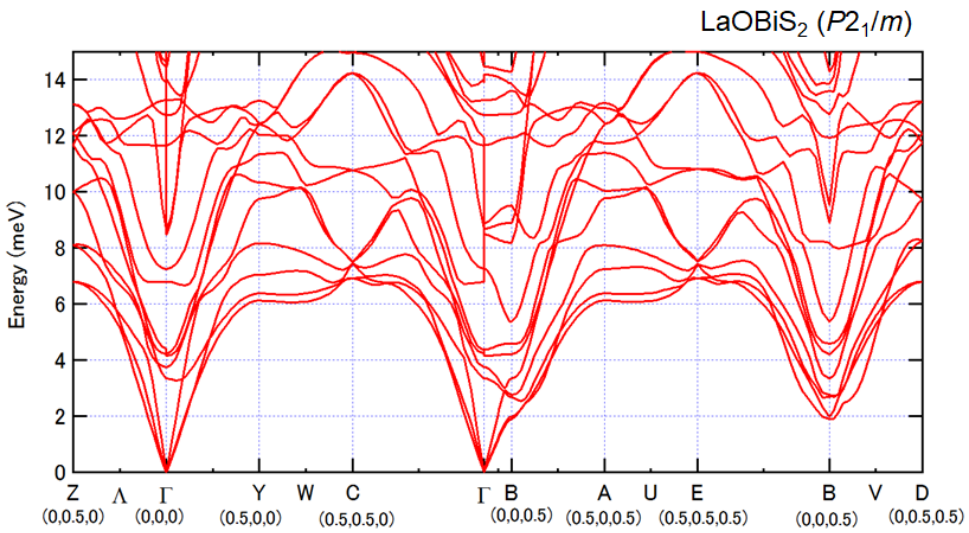

Figure 15. Phonon band structure for $LaOBiS_2$. The original data has been published in Ref. 44, and this figure is a modified output. Because of structural instability, we assumed monoclinic ($P2_1/m$) structure, which was more stable than tetragonal in the calculation.

To confirm the validity of the analysis with the combination of multiple models, we show calculation results of C/T^3 in Fig. 14(a). The original data of the calculation of phonons have been published in Ref. 44. The calculation is based on the monoclinic ($P2_1/m$) structure; $LaOBiS_{2-x}Se_x$ undergoes structural transition from tetragonal ($P4/nmm$) to monoclinic [3]. In contrast, F-doped $LaO_{0.5}F_{0.5}BiS_{2-y}Se_y$ does not undergo the structural transition, and the tetragonal structure remains at low temperatures [58]. However, the monoclinicity in this system is quite small, and the affections of the structural symmetry lowering to phonon characteristics are limited. Therefore, we use the result as a reference. The calculated C/T^3-T exhibits a trend quite similar to the experimental result. The difference is the presence/absence of the low-T upturn in experimental and calculated results, which would be due to the presence of local structural disorders that cannot be incorporated into the calculations. Another difference is the absolute values of the peak amplitude. The calculated peak height is higher than that obtained by the experiment; this difference would also be caused by the in-plane disorder because the inconsistency is removed by Se substitution. Figure 14(b) shows the phonon DOS with the contributions from Bi. The phonon band structure is displayed in Fig. 14. It is clear that the phonon DOS below 10 meV are dominated by Bi vibrations. Figures 14(c) and 14(d) show typical displacement modes at E = 3.4 and 7.4 meV, respectively, with arrows showing atomic displacements. Since Bi is quite heavier than S and O, the size of the

arrows becomes smaller than that of the others, but there are clear Bi vibrations seen in those figures. We consider that the two Einstein modes with θ_{E1} = 78 K and θ_{E2} = 35 K (Table I) are corresponding to those modes of Bi vibrations.

Now, we discuss the results for the phonons of LaOBiSSe (x = 1.0) where the in-plane S1 site is selectively substituted by Se with full occupancy. The analysis with double Debye and triple Einstein models similar to model 4 [Fig. 14(f)] is applied, and the result is shown in Fig. 16. The used model parameters are listed in Table II. With Se substitution, θ_{D1} and θ_{D2} decrease, and θ_{E1} slightly decreases, which is consistent with the peak shift in C/T^3-T between $LaOBiS_2$ and LaOBiSSe. The noticeable trend is the increase in n_{E1} and n_{E2} by the Se substitution. Instead of that, n_{D1} is reduced, which implying the increase in the oscillator number of the optical phonon modes and the stabilization of the modes by the in-plane chemical pressure effects. Because $LaOBiS_2$ possesses huge local structural disorders in the conducting plane [33], we consider that the suppression of the disorder is essential for the emergence of intrinsic Bi vibrations expected from the phonon calculations. In the other words, in the Se-free Bi-S1 planes with local disorders, the Bi vibrations along the c-axis are largely suppressed by the local disorder, which results in the smaller n_{E1}. As a fact, the experimental value of the peak of C/T^3 is almost the same as the calculated value. This scenario is consistent with previous works on X-ray absorption spectroscopy, which reported on a large change in the bonding states of the Bi-S1-plane from glassy to crystalline by Se substitution [33]. The stabilization of the large-amplitude Bi vibrations along the c-axis should be linked to the suppression of thermal conductivity, which is a key factor for the high ZT.

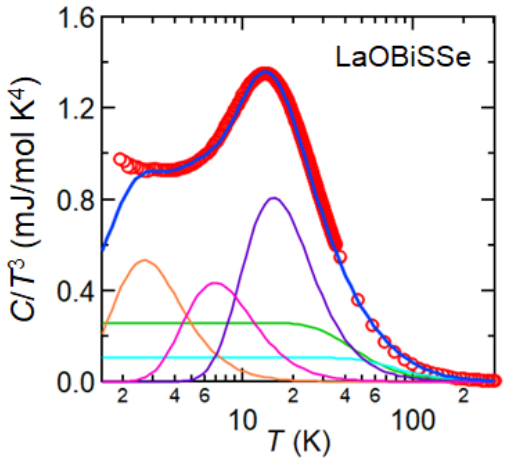

Fig. 16. Temperature dependence of C/T^3 for LaOBiSSe. The horizontal axis is in log scale. Double Debye and triple Einstein models are assumed [57].

Table II. The parameters used for the C/T^3 analyses with model 4 for $LaOBiS_2$ and LaOBiSSe.

Model parameter	$LaOBiS_2$	LaOBiSSe
θ_{D1} (n_{D1})	223 K (n = 1.46195)	218 K (n = 1.3258)
θ_{D2} (n_{D2})	450 K (n = 3)	380 K (n = 3)
θ_{E1} (n_{E1})	78 K (n = 0.51)	75 K (n = 0.64)
θ_{E2} (n_{E2})	35 K (n = 0.026)	34 K (n = 0.032)
θ_{E3} (n_{E3})	13 K (n = 0.00205)	13 K (n = 0.0022)

Case 2

Case 2 assumes n_{D1} : n_{D2} = 10/3 : 5/3 where we assume the difference of transverse and longitudinal sound velocities. Because of the large n_{D1} (lower θ_D), the θ_D estimated from low-T fitting could not be used, and higher θ_Ds are needed. The analyses results are shown in Fig. 17 and Table III. However, as shown in Table III, the trend of n_{E1} corresponding to the Bi c-axis vibration is common to case 1; n_{E1} increases by Se substitution. Therefore, we concluded that the use of both case 1 and 2 can be useful for extracting the effect of in-plane CP on the Bi vibration along the c-axis. Because this analysis is based on many variable parameters, reducing variable parameters is ideal. Therefore, we use case 1 with fixed the lower θ_D determined by low-T fitting in the investigation on superconducting $LaO_{0.5}F_{0.5}BiS_{2-x}Se_x$ samples with carrier doping.

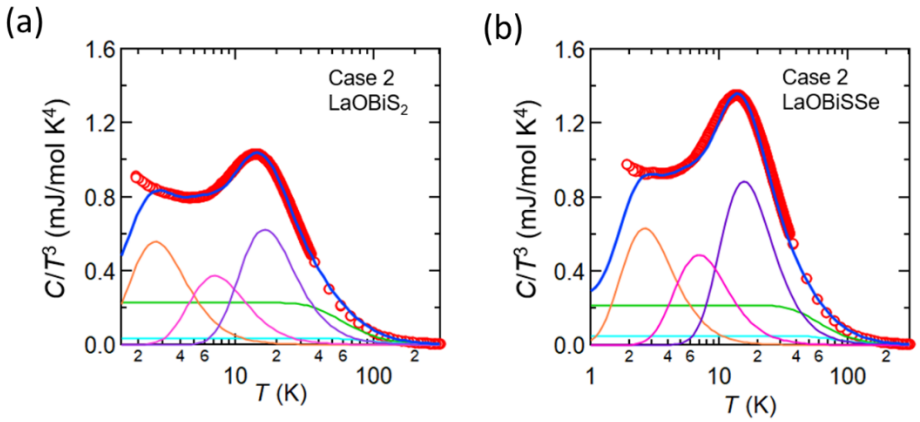

Fig. 17. Temperature dependence of C/T^3 for $LaOBiS_2$ and LaOBiSSe in case 2. The horizontal axis is in log scale.

Table III. The parameters used for the C/T^3 analyses in case 2 with model 4 for $LaOBiS_2$ and LaOBiSSe.

Model parameter	$LaOBiS_2$	LaOBiSSe
θ_{D1} (n_{D1})	285 K (n = 2.70)	285 K (n = 2.57)
θ_{D2} (n_{D2})	450 K (n = 1.667)	400 K (n = 1.67)
θ_{E1} (n_{E1})	80 K (n = 0.60)	76 K (n = 0.73)
θ_{E2} (n_{E2})	35 K (n = 0.030)	34 K (n = 0.036)
θ_{E3} (n_{E3})	13 K (n = 0.0023)	13 K (n = 0.0026)

4.3 $LaO_{0.5}F_{0.5}BiS_{2-x}Se_x$

On the basis of the discussion above, we analyzed specific heat data for F-substituted $LaO_{0.5}F_{0.5}BiS_{2-x}Se_x$ (x = 0, 1.0) superconducting samples using model 4 of case 1. In Fig. 18, the results of the analyses of C_{lat}/T^3 are displayed. C_{lat} was obtained by $C_{lat} = C - \gamma T$, where γ is an electronic specific heat coefficient and determined by low-T fitting of C/T-T^2 to $C/T = \gamma + \beta T^2$. We used data taken at H = 3 T for T < 5 K to avoid the contribution from superconducting states. We confirmed that the low-T (H = 3 T) data are smoothly connected to the higher-T data. In La(O,F)BiS_2, a previous study showed that the low-energy phonon DOS are not largely affected by F substitution [38].

As shown in Fig. 18(a), the T-dependence of C_{lat}/T^3 for $LaO_{0.5}F_{0.5}BiS_2$ is well fitted with model 4. Here, γ = 0.96(2) mJ/mol K^2 is used for $LaO_{0.5}F_{0.5}BiS_2$. The results are quite similar to $LaOBiS_2$, where the peak amplitude for the optical phonon contribution with θ_{E1} is relatively smaller than that in the calculation. Since the oscillator number n_{E1} is around 0.5 for $LaOBiS_2$ and $LaO_{0.5}F_{0.5}BiS_2$, the difference between the experimental data and the calculation result is basically caused by the small n_{E1}. Figure 18(b) shows the analysis result for $LaO_{0.5}F_{0.5}BiSSe$ with model 4. The γ is 2.71(4) mJ/mol K^2 for $LaO_{0.5}F_{0.5}BiSSe$. As compared to $LaO_{0.5}F_{0.5}BiS_2$, the experimental values are close to the calculation result, particularly at the optical-phonon peak. The trend of the affection by the Se substitution at the in-plane S1 site is quite similar to the case of LaOBiSSe. The n_{E1} increases from 0.52 (for $LaO_{0.5}F_{0.5}BiS_2$) to 0.60 (for $LaO_{0.5}F_{0.5}BiSSe$). Because of the almost same θ_{E1} for both analyses, the increase in n_{E1} should

be an essential feature caused by the in-plane CP effects. On the superconductivity in $LaO_{0.5}F_{0.5}BiS_{2-x}Se_x$, bulk nature of superconductivity is enhanced by Se substitution [9,24,59]. Although the Debye and Einstein temperatures decreases with Se substitution, γ increases with Se substitution. Therefore, we cannot simply discuss the cause of the enhanced superconducting properties by the Se substitution in $LaO_{0.5}F_{0.5}BiS_{2-x}Se_x$ in the frame work of the conventional phonon-mediated mechanism [60]. However, the fact that the enhancement of bulk nature occurs when the Bi vibration along the c-axis with θ_{E1} is stabilized suggest positive relationship between the Bi vibration and superconductivity. Therefore, investigation on phonons at low temperatures is needed to further understand the relationship.

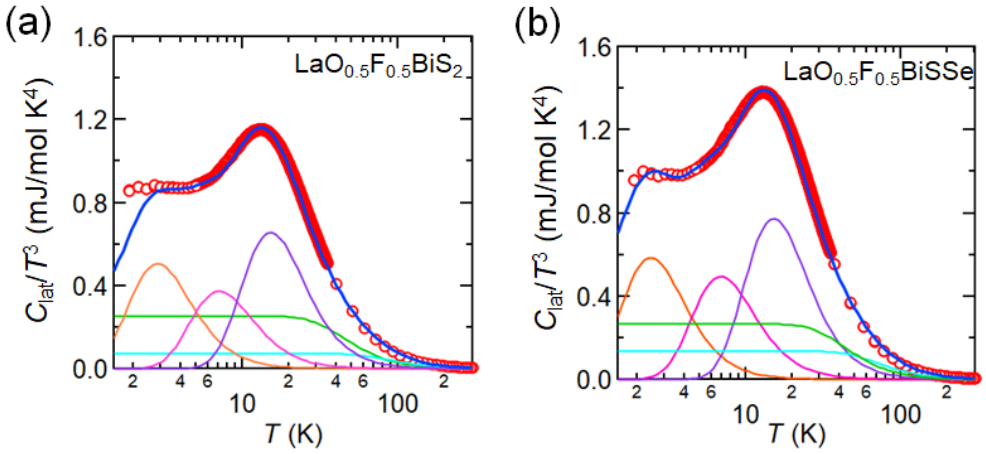

Fig. 18. Temperature dependence of C_{lat}/T^3 for $LaO_{0.5}F_{0.5}BiS_2$ and $LaO_{0.5}F_{0.5}BiSSe$. The horizontal axis is in log scale. Double Debye and triple Einstein models are assumed [57].

Table IV. The parameters used for the C_{lat}/T^3 analyses for all the examined samples with model 4 in case 1.

Model parameter	**$LaOBiS_2$**	**LaOBiSSe**	**$LaO_{0.5}F_{0.5}BiS_2$**	**$LaO_{0.5}F_{0.5}BiSSe$**
θ_{D1} (n_{D1})	223 K (n = 1.46195)	218 K (n = 1.3258)	223 K (n = 1.4474)	218 K (n = 1.3616)
θ_{D2} (n_{D2})	450 K (n = 3)	380 K (n = 3)	430 K (n = 3)	350 K (n = 3)
θ_{E1} (n_{E1})	78 K (n = 0.51)	75 K (n = 0.64)	75 K (n = 0.52)	74.5 K (n = 0.60)
θ_{E2} (n_{E2})	35 K (n = 0.026)	34 K (n = 0.032)	35 K (n = 0.03)	34 K (n = 0.0365)
θ_{E3} (n_{E3})	13 K (n = 0.00205)	13 K (n = 0.0022)	14 K (n = 0.0026)	12 K (n = 0.0019)

5. Grüneisen parameter

In chapter 4, we concluded that the in-plane CP effects stabilize Bi large amplitude vibration along the *c*-axis. Because lattice anharmonicity was theoretically indicated for $LaOBiS_2$ [35], we considered that lattice anharmonicity is also enhanced by the stabilization of the Bi vibration along the *c*-axis. Here, we used Grüneisen parameter (γ_G) to investigate the change in lattice anharmonicity by in-plane CP effects.

5.1 Introduction

The Grüneisen parameter [61] is a dimensionless thermodynamic parameter named after a German physicist Eduard Grüneisen. Its original definition was formulated in terms of phonon nonlinearities. Because different properties and derivatives in thermodynamics are equivalent, like in the Maxwell Relations, there are different ways to write the γ_G that are all correct [62]. As a result, there are numerous interpretations of its meaning. Here are some formulations for the Grüneisen parameter:

$$\gamma_G = V\left(\frac{dP}{dE}\right)_v = \frac{\alpha K_T}{C_P \rho} = \frac{\alpha K_T}{C_V \rho} = \frac{\alpha V_s^2}{C_P} = -\left(\frac{\partial lnT}{\partial lnV}\right)_S \qquad (5\text{-}1)$$

Here, V, C_p, C_v, E, S, α, and ρ are volume, heat capacity constant pressure, heat capacity constant volume, energy, entropy, volumetric thermal expansion coefficient, and density, respectively.

In this chapter, we discuss how γ_G changes with in-plane CP for the thermoelectric $LaOBiS_{2-x}Se_x$ [63], and the superconducting phases of $LaO_{0.5}F_{0.5}BiS_{2-x}Se_x$ [64], and $RE(O,F)BiS_2$ [65] . In our study we use the equation (5-2) used in Ref. 66,67.

$$\gamma_G = \frac{\beta_V B V_{mol}}{C_V} \qquad (5\text{-}2)$$

where β_V, B, V_{mol}, and C_V are volume thermal expansion coefficient, bulk modulus, molar volume, and specific heat, respectively. The parameters needed for the estimation of γ_G are

calculated as follows (formula 5-3–6). In the formulas, dV/dT, ρ, v_L, v_S, v_m, θ_D, h, k_B, n, N_A, and M denote temperature gradient of lattice volume, density of the material, longitudinal sound velocity, shear sound velocity, average sound velocity, Debye temperature, Plank's constant, Boltzmann's constant, number of atoms in the molecule (formula unit), Avogadro's constant, and the molecular weight (per formula unit).

$$\beta_V = \frac{1}{V(300\ \mathrm{K})}\frac{dV}{dT} \tag{5-3}$$

$$B = \rho\left(v_L^2 - \frac{4}{3}v_S^2\right) \tag{5-4}$$

$$\theta_D = \left(\frac{h}{k_B}\right)\left[\frac{3n}{4\pi}\left(\frac{N_A\rho}{M}\right)\right]^{\frac{1}{3}} v_m \tag{5-5}$$

$$v_m = \left[\frac{1}{3}\left(\frac{2}{v_S^3} + \frac{1}{v_L^3}\right)\right]^{-\frac{1}{3}} \tag{5-6}$$

5.1 $LaOBiS_{2-x}Se_x$

We estimated γ_G for the HP-annealed samples of $LaOBiS_2$ (x = 0) and LaOBiSSe (x = 1.0). From specific heat analyses, we revealed that Se substitution stabilizes Bi vibration along the c-axis. We evaluated volumetric thermal expansion β_V using volume measured by synchrotron XRD (example pattern is shown in Fig. 19) at T = 100–400 K as shown in Figs. 20(a,d). The experimental value of C (T = 300 K)was estimated using experimental values. The obtained parameters and γ_G is listed in Table V. Although the absolute values depend on the used θ_D, the trend that γ_G increases by Se substitution is common. The increase in γ_G indicates the enhancement of lattice anharmonicity in $LaOBiS_{2-x}Se_x$.

Table V. Parameters estimated using lower θ_D estimated from low-T fitting [Fig. 13(a)] and average θ_D estimated using equation (4-4).

Measured value	$LaOBiS_2$		LaOBiSSe	
β_V (μK^{-1}) at 300 K	15.8	15.8	24.5	24.5
C (J/Kmol) at 300 K	108	108	112	112
Relative density (HP-annealed) (%)	94.4	94.4	94.4	94.4
θ_D (K) (lower)	223		218	
θ_D (K) (average)		286		272
V_L (m/s) at 300 K	3060	3060	3170	3170
Calculation results				
B (GPa)	36.4	13.9	46.7	25.2
γ_G	0.34	0.13	0.65	0.37

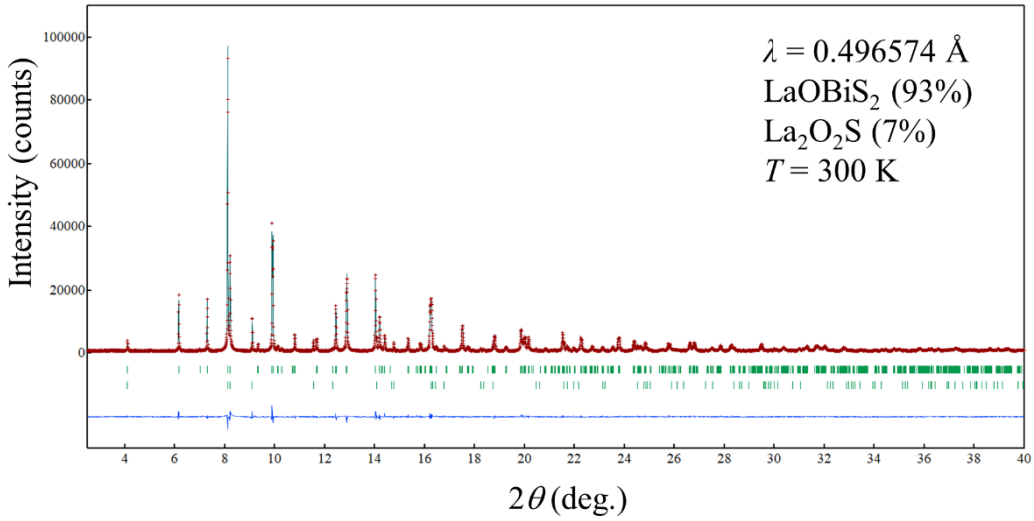

Fig. 19. SXRD pattern for $LaOBiS_2$ at $T = 300$ K.

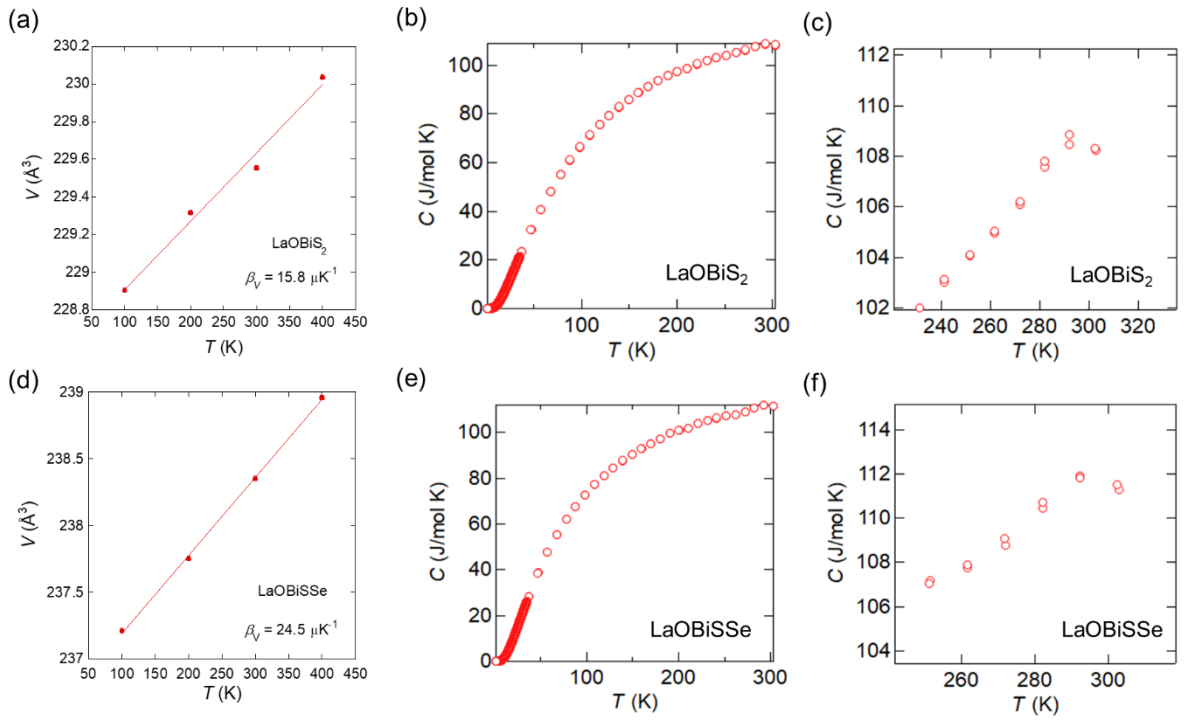

Fig. 20. (a,d) T dependence of V for (a) $x = 0$ and (d) 1.0. (bc,e,f) T dependence of C and zoomed figure at high temperatures for (b,c) $x = 0$ and (e,f) 1.0.

5.3 $LaO_{0.5}F_{0.5}BiS_{2-x}Se_x$

We first investigated superconducting properties to confirm reproducibility. The magnetization and specific heat experiments were carried out in order to explore the superconducting characteristics of the samples. The magnetic susceptibility ($4\pi\chi$) was calculated from the obtained magnetization data as depicted in Figure 21(a). For $x = 0$, almost no shielding signals were observed as shown in Fig. 21(b). When x is equal to 0.2, the shielding volume fraction (ZFC) data does not reach -1. Having considered the fact that the material studied here is polycrystalline sample of layered compound, shielding fraction greater than 100% is expected from the demagnetization effect (crystal shape effect) [24]. Therefore, we roughly judge that samples with $x > 0.4$ are non-bulk superconducting samples. The trend is consistent with a previous study [24], and Se substitution leads to bulk superconductivity in this system. The superconductivity phase diagram is shown in Fig. 24(a).

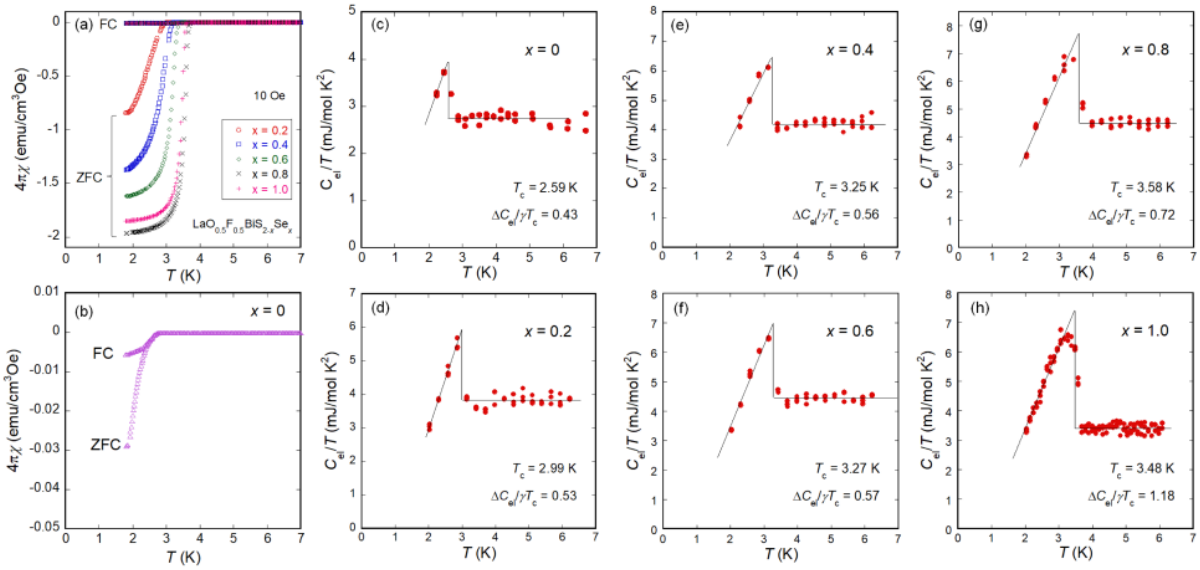

Figure 21. Superconducting properties of the $LaO_{0.5}F_{0.5}BiS_{2-x}Se_x$. (a, b) Temperature dependences of zero field cooling (ZFC) and field cooling (FC) magnetic susceptibility ($4\pi\chi$). (c–h) Temperature dependences of electronic specific heat (C_{el}) in a form of C_{el}/T.

Figures 21(c–h) illustrate the temperature dependences of C_{el}/T, where C_{el} is the electronic specific heat and was determined by subtracting phonon contribution. These temperature dependences are displayed in the context of the specific heat. We made the assumption that the expression $C = \gamma T + \beta T^3 + \delta T^5$ gave an appropriate description of the low-temperature C. The T_c in the specific heat measurements is estimated according to the studies of the jump of C_{el} at T_c (C_{el}) where the entropy balance was taken into consideration. The value of $\Delta C_{el}/\gamma T_c$ for $x = 0$ is small, which is consistent with quite small shielding volume fraction in magnetic susceptibility data. The $\Delta C_{el}/\gamma T_c$ remains almost comparable when x is equal to 0, 2, 0,4, and 0,6; however, it begins to increase when x is equal to 0.8 and 1.0. The estimated value for $x = 1.0$ is approaching the value expected from the BCS model. As well, shielding volume fraction is also enhanced for Se-rich compositions.

Then, we estimate γ_G for those samples. Fig. 22 illustrates the SXRD pattern and the refinement result for $x = 0.8$ at $T = 301$ K. Despite the small LaF_3 impurity, the SXRD pattern was well fitted by tetragonal $P4/nmm$ model. The compositions determined by EDX are listed in Table VI. We show a typical data set of $x = 0.8$, and the estimated physical parameters are summarized in Table VI. As shown in Fig. 24(b), in-plane CP increases by Se substitution, but bulk modulus saturate as shown in Fig. 23(c). As a result, the increase in γ_G is limited, but γ_G slightly increases from $x = 0$ to $x > 0.4$. This trend may be related with the small increase in n_{El}

from x = 0 to x = 1.0 in $LaO_{0.5}F_{0.5}BiS_{2-x}Se_x$ as compared to the $LaOBiS_{2-x}Se_x$ case where the clear increase in n_{E1} is observed by Se substitution.

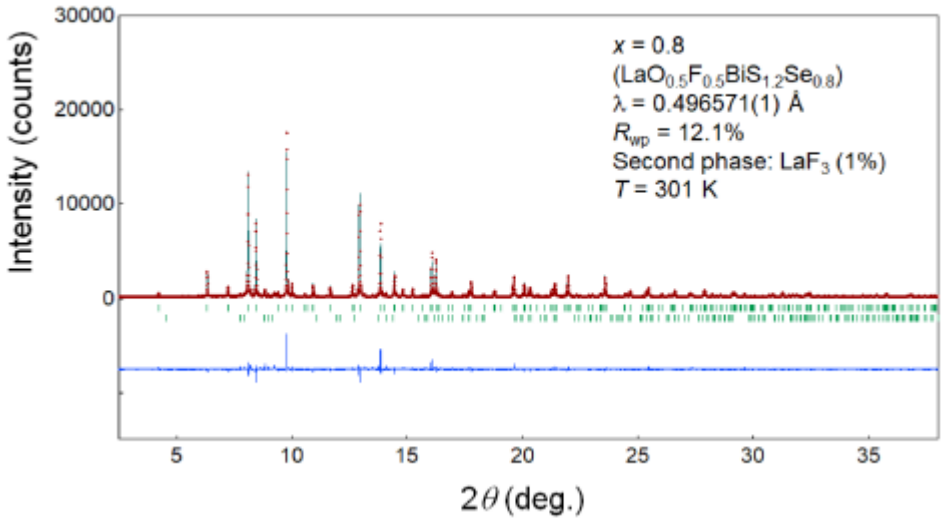

Figure 22. SXRD pattern and Rietveld refinement result for x = 0.8.

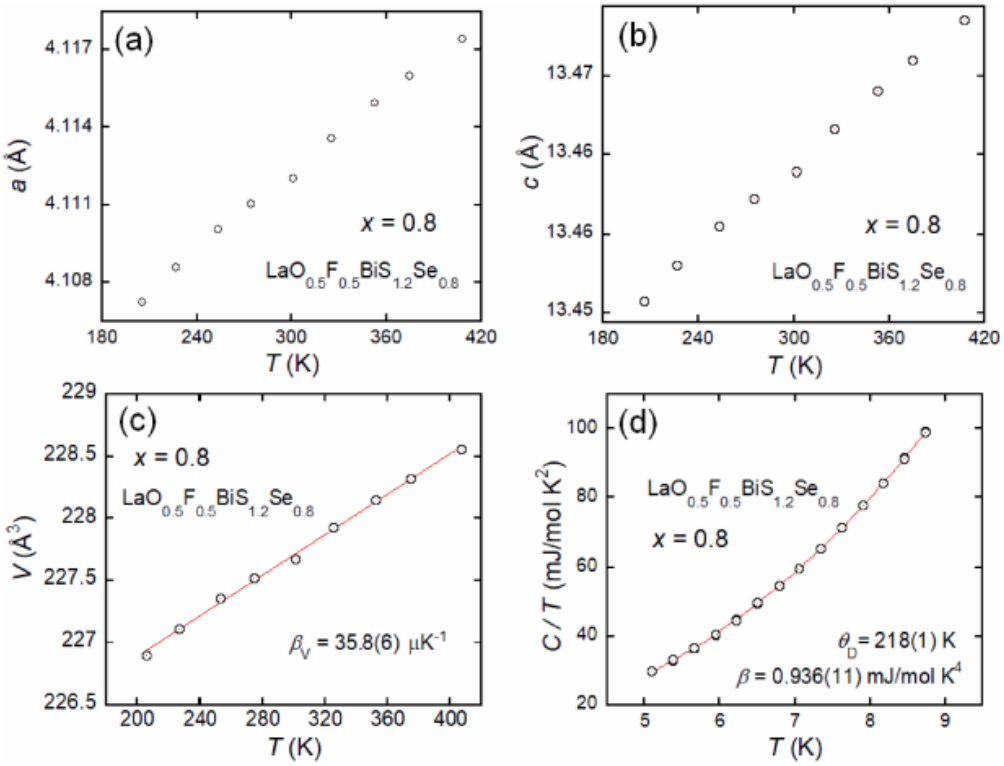

Figure 23. (a–c) Temperature dependences of the two-lattice constant and the cell volume for x = 0.8 are a, c, and V, are plotted respectively. (d) Fitting result of specific heat, C is plotted using $C = \gamma T + \beta T^3 + \delta T^5$.

Table VI. Parameters needed for the estimation of γ: composition, ideal density (ρ), relative density, volume thermal expansion coefficient (β_V), bulk modulus (B), calculated lattice vibration heat capacity value at 300 K (C_V), Debey temperature (θ_D), corrected longitudinal, shear, and average sound velocities (v_L, v_s, and v_m), and γ_G.

Nominal x	0.2	0.4	0.6	0.8	1.0
x (EDX)	0.131(8)	0.40(2)	0.600(11)	0.778(10)	0.969(14)
Refined x	0.16(2)	0.44(2)	0.61(2)	0.87(2)	1.00(2)
Space group	Tetragonal $P4/nmm$ (#129)				
Relative density (%)	96	96	96	98	98
a (Å) ($T \sim 300$ K)	4.07513(5)	4.08667(4)	4.10009(6)	4.11241(4)	4.12604(5)
c (Å) ($T \sim 300$ K)	13.3792(2)	13.4101(2)	13.4367(3)	13.4622(2)	13.5116(2)
V (Å^3) ($T \sim 300$ K)	222.184(5)	223.960(5)	225.882(6)	227.672(4)	230.024(6)
In-plane CP	1.015	1.021	1.026	1.031	1.035
β_V (μK^{-1})	35.8(4)	35.9(6)	39.6(6)	35.8(6)	36.7(5)

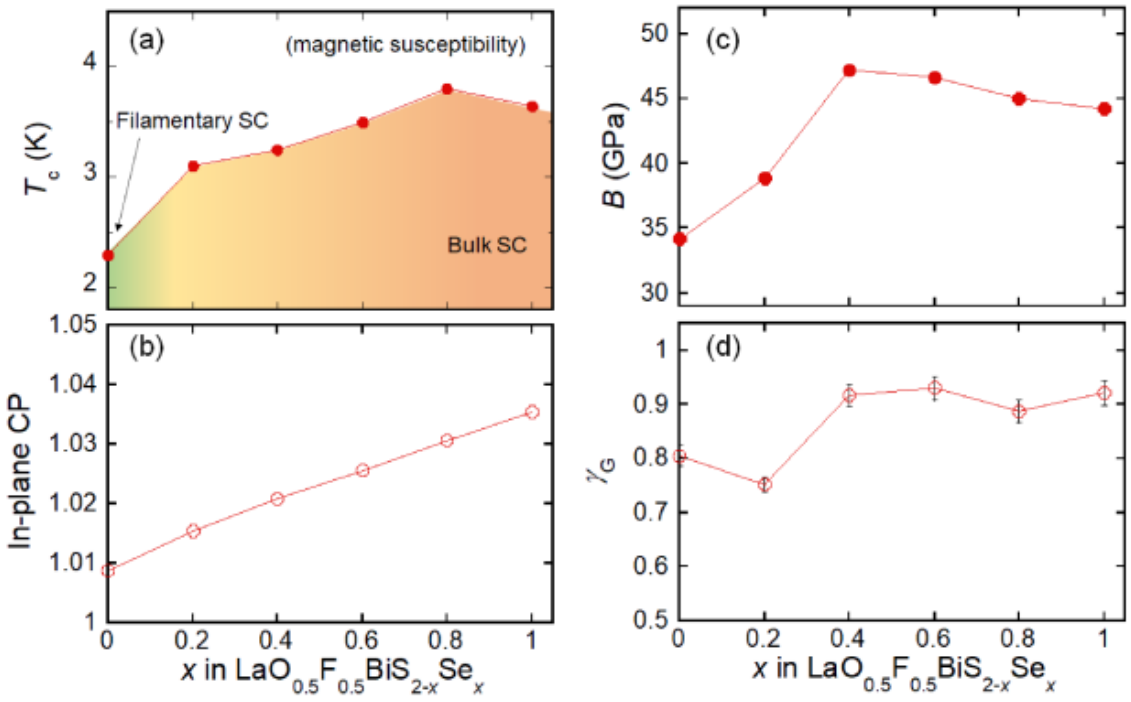

Figure 24. Se concentration (x) dependences of (a) T_c (magnetic susceptibility), (b) in-plane CP (c) bulk modulus (B), and (d) γ_G.

5.4 $REO_{0.5}F_{0.5}BiS_2$

As introduced in the introduction parts, in-plane chemical pressure effects are essential for the emergence of bulk superconductivity in the $RE(O,F)BiS_{2-x}Se_x$ systems, and the substitution of La by smaller RE results in positive in-plane CP effects. In this section, we show the relationship between in-plane CP and γ_G for $RE(O,F)BiS_2$.

Figure 25 shows the SXRD patterns for the $RE(O,F)BiS_2$ samples taken at $T = 600$ K as well as the Rietveld refinement results. Tiny impurity phases of REF_3 (RE = La, Ce, Pr, Nd) were assumed in the refinements. Figures 26(a–e) show the T dependence of V. The β_V for $LaO_{0.5}F_{0.5}BiS_2$, $CeO_{0.5}F_{0.5}BiS_2$, $PrO_{0.5}F_{0.5}BiS_2$, $NdO_{0.5}F_{0.5}BiS_2$, and $NdO_{0.7}F_{0.3}BiS_2$, are 39.6, 32.9, 38.4, 37.8, and 36.4 μK^{-1}, respectively. In addition, T dependences of isotropic atomic displacement parameters (U_{iso}) are shown in Figs. 26(g–j) to confirm the suppression of disorder (atomic displacements) at the S1 site. For RE = Nd, U_{iso} (S1) is clearly suppressed.

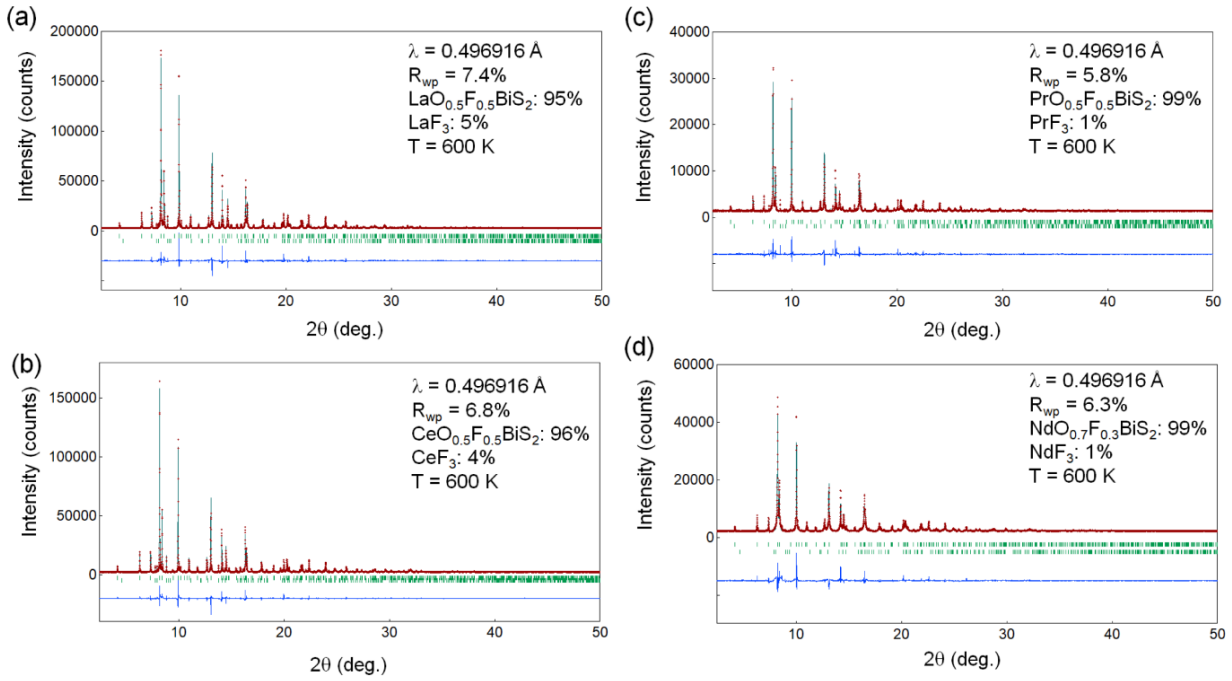

Figure 25. SXRD patterns and Rietveld refinement results for (a) $LaO_{0.5}F_{0.5}BiS_2$, (b) $CeO_{0.5}F_{0.5}BiS_2$, (c) $PrO_{0.5}F_{0.5}BiS_2$, and (d) $NdO_{0.7}F_{0.3}BiS_2$ for T=600 K.

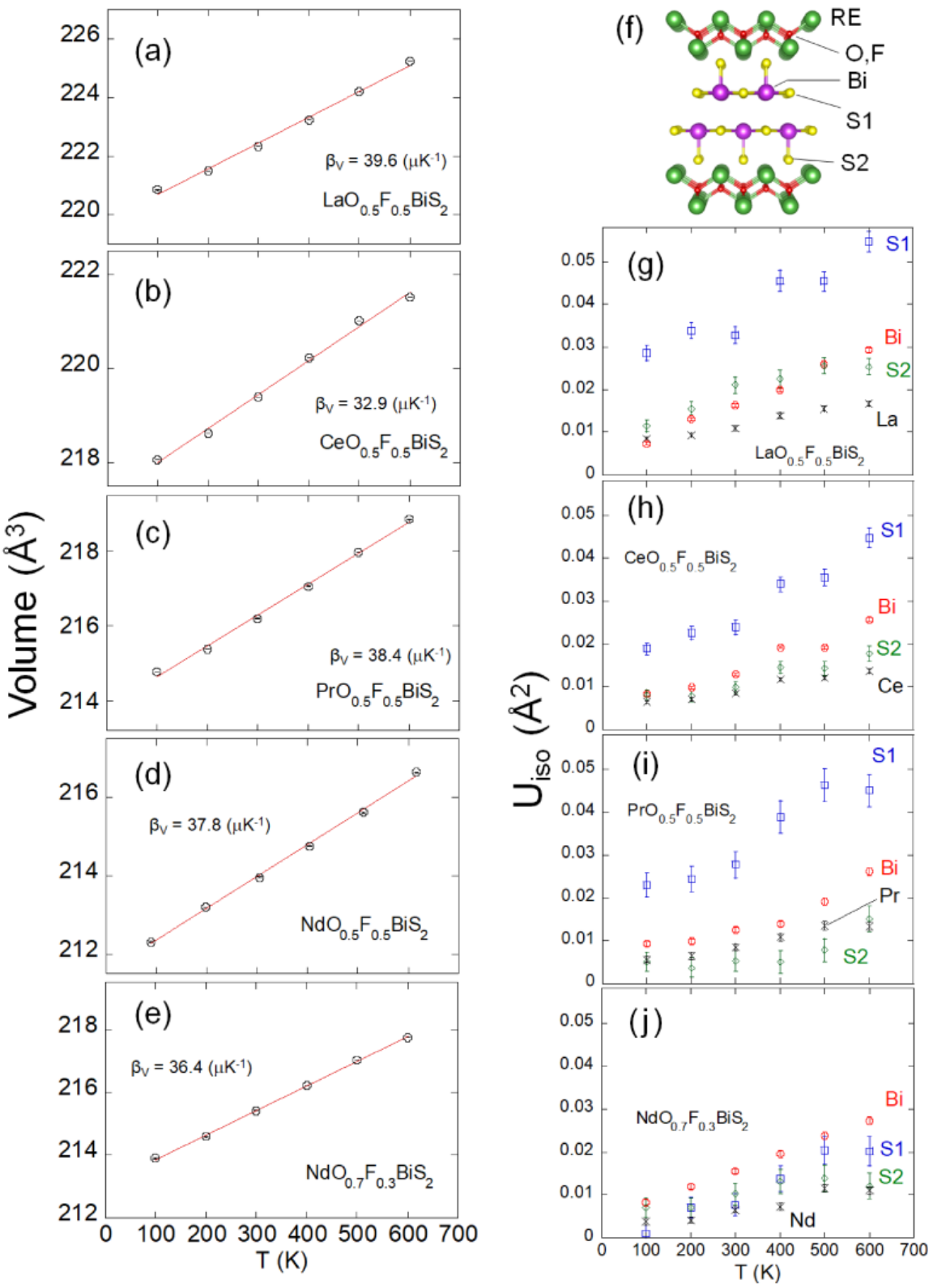

Figure 26. Temperature dependence of lattice volume (*V*) (a-e), schematic image (f) and Temperature dependence of isotropic atomic displacement for $REO_{0.5}F_{0.5}BiS_2$ (RE = La, Ce, Pr, Nd), respectively.

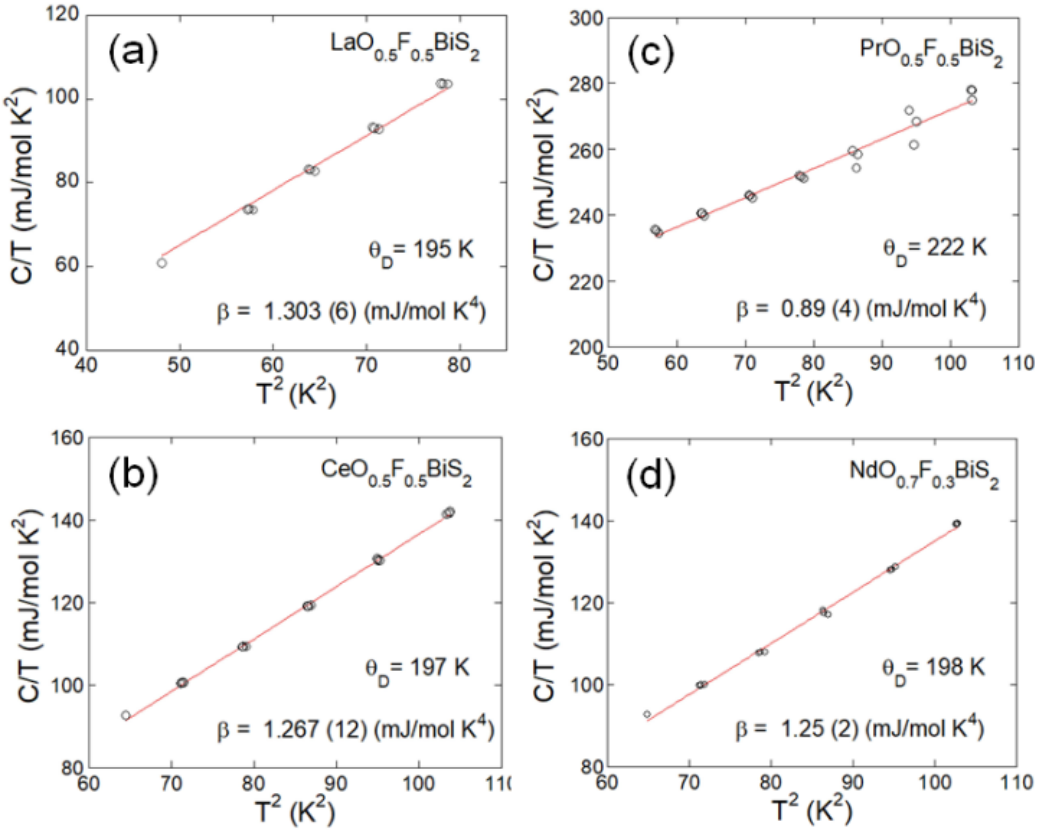

Figure 27. T^2 dependence of C/T for (a-d) $REO_{0.5}F_{0.5}BiS_2$ (RE= La, CE, Pr, Nd).

The dependence of C/T on T^2 is shown in Figs. 27(a-d), and θ_D is estimated to be 195(1), 197(1), 222(3), and 198(1) K for $LaO_{0.5}F_{0.5}BiS_2$, $CeO_{0.5}F_{0.5}BiS_2$, $PrO_{0.5}F_{0.5}BiS_2$, $NdO_{0.5}F_{0.5}BiS_2$, respectively. However, we found that the analysis of θ_D for RE = La was better when the δT^5 term was added in the analysis; in the calculation of γ_G, we used 228(1) K for RE = La, which is consistent with the detailed measurements at low temperatures shown in Table IV. A large θ_D that was obtained when RE = Pr is in line with findings from previous studies [68]. In the case of $NdO_{0.5}F_{0.5}S_2$, the value of θ_D was formerly estimated to be 189 K [69].

Figure 28 illustrates the plot of the bulk modulus (B). The value of B increases with decreasing RE ionic radius from La to Nd. This tendency would be attributed to the fact that when the lattice constant decreases, the in-plane CP increases. The following is the formula that should be used to calculate the value of B: $B = -V_0(dP/dV)$, where V_0 is the volume in the starting state and dP/dV is the change in internal pressure owing to the change in volume. The observation of the clear increase in B with increasing in-plane chemical pressure in the

$REO_{0.5}F_{0.5}BiS_2$ system is different from the results in $LaO_{0.5}F_{0.5}BiS_{2-x}Se_x$ in which the increase in B is saturated at the middle in-plane CP effects.

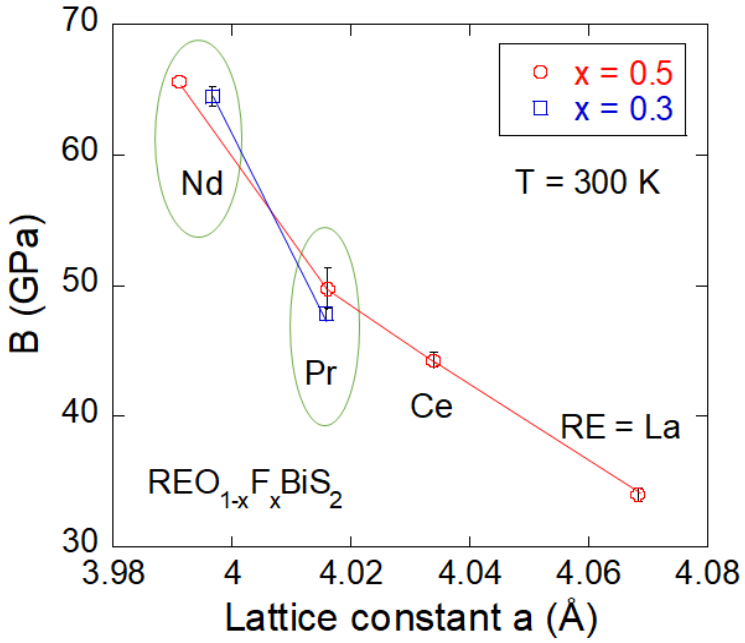

Figure 28. Lattice constant (*a*) dependence of bulk modulus (*B*) for $T = 300$ K.

We estimated γ_G for the $REO_{1-x}F_xBiS_2$ samples (here, $x = 0.3$ data are also shown) and plotted in Fig. 29 with superconductivity phase diagram. The obtained parameters are summarized in Table VII. In the system, bulk superconductivity emerges for RE = Pr and Nd. At that, γ_G increases with decreasing RE^{3+}-site ionic radius. Similar trend was observed in $x = 0.3$ samples. We conclude that bulk superconductivity is induced when lattice anharmonicity was enhanced in the $REO_{1-x}F_xBiS_2$ samples. Although the phonon estimation for $REO_{1-x}F_xBiS_2$ is difficult due to the appearance of RE-4f contribution on low-T specific heat [70], we expect the stabilization of the Bi vibration along the c-axis in the $REO_{1-x}F_xBiS_2$ system. To clarify the relationship between superconductivity, Bi vibration, and lattice anharmonicity, further investigation is needed.

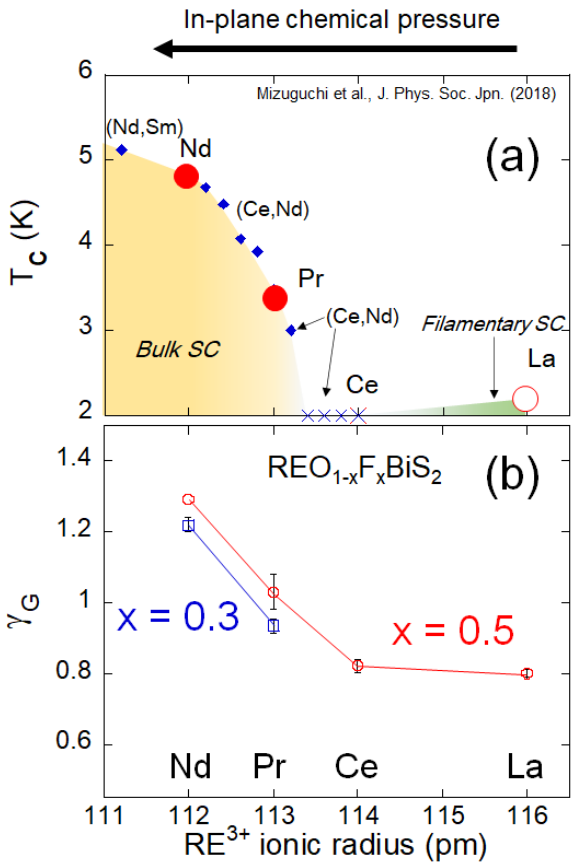

Figure 29. RE^{3+} ionic radius dependence of (a) T_c for $REO_{0.5}F_{0.5}BiS_2$ (x =0.5) and (b) estimated γ_G for $REO_{0.5}F_{0.5}BiS_2$.

Table 2. Parameters needed for the estimation of γ: composition, ideal density (ρ), relative density, volume thermal expansion coefficient (β_V), bulk modulus (B), calculated lattice vibration heat capacity value at 300 K (C_V), Debey temperature (θ_D), corrected longitudinal, shear, and average sound velocities (v_L, v_s, and v_m), and γ_G.

RE	La	Ce	Pr	Nd	Nd
F contents (x)	0.5	0.5	0.5	0.5	0.3
Relative density (%)	100	100	97.8	96.0	94.9
β_V (μK^{-1})	39.6(8)	32.9(11)	38.4(11)	37.8(8)	36.4(5)
v_L (exp) (m/s)	3330(10)	3320(10)	3450(10)	3470(10)	3450(10)
v_L (ideal) (m/s)	3330	3320	3527	3616	3635
v_S (ideal) (m/s)	1997	1687	1875	1567	1640
v_m (ideal) (m/s)	2209	1890	2096	1770	1850
θ_D (K)	228(1)	197(1)	222(3)	189	198(1)
B (GPa)	34.2(5)	44.3(6)	49.8(16)	65.6	64.5(8)
C_V (J/K mol)	124.6	124.6	124.6	124.6	124.6
γ_G	0.81(1)	0.82(2)	1.03(5)	1.29	1.22(2)

6. Conclusions

We studied the effects of in-plane CP on the optical phonons corresponding to the Bi large-amplitude vibration along the *c*-axis by analyzing lattice specific heat for $BiCh_2$-based compounds. For non-carrier-doped system $LaOBiS_{2-x}Se_x$, a clear stabilization of Bi vibration along the *c*-axis with low optical phonon energy was observed by Se substitution. In addition, for $LaOBiS_2$, the C/T^3 values exhibit smaller values than that calculated from phonon band structure, and it becomes values close to the calculated values by Se substitution in LaOBiSSe. The stabilization of the Bi vibration is suggested from the increase in oscillator number strength (n_{E1}) for the corresponding Einstein mode. Those results indicate that the Bi vibration is suppressed in $LaOBiS_2$ possibly due to the presence of in-plane local disorder, and the in-plane CP effect, which suppresses the in-plane disorder, stabilizes the Bi vibration. Similar trend was observed in electron-doped (superconducting) $LaO_{0.5}F_{0.5}BiS_{2-x}Se_x$. Although the change in n_{E1} by Se substitution was smaller than the $LaOBiS_{2-x}Se_x$ case, an increase in n_{E1} was observed by Se substitution.

Because low-energy optical phonon would contribute to the enhancement of lattice anharmonicity in materials, we estimated the effects of in-plane CP on lattice anharmonicity by estimating Grüneisen parameter (γ_G). For $LaOBiS_{2-x}Se_x$, a clear increase in γ_G by Se substitution was observed. In the case of $LaO_{0.5}F_{0.5}BiS_{2-x}Se_x$, the increase in γ_G by Se substitution was small, but it would be consistent with the result on the small increase in n_{E1} in the specific heat analysis. In addition, we investigated the in-plane CP effects on γ_G in $RE(O,F)BiS_2$, and observed a clear correlation between in-plane CP and γ_G. Therefore, the in-plane CP on the in-plane Bi-Ch1 bond commonly linked to the lattice anharmonicity.

Thorough the investigation of optical phonon by specific heat analyses and lattice anharmonicity by γ_G, we found the correlation between in-plane CP, Bi large-amplitude vibration along the *c*-axis, and lattice anharmonicity. The obtained knowledge enrich the understanding of the vibrational characteristics along the *c*-axis, which had not been studied in detail. However, to deepen the discussion on the correlation between superconducting mechanism and those vibrational factors, further investigation on phonons using low-*T* probes is needed.

References

1. Y. Mizuguchi, H. Fujihisa, Y. Gotoh, K. Suzuki, H. Usui, K. Kuroki, S. Demura, Y. Takano, H. Izawa, and O. Miura, Phys. Rev. B 86, 220510 (2012).
2. Y. Mizuguchi, S. Demura, K. Deguchi, Y. Takano, H. Fujihisa, Y. Gotoh, H. Izawa, and O. Miura, J. Phys. Soc. Jpn. 81, 114725 (2012).
3. Y. Mizuguchi, J. Phys. Soc. Jpn. 88, 041001 (2019).
4. H. Takatsu, Y. Mizuguchi, H. Izawa, O. Miura, and H. Kadowaki, J. Phys. Soc. Jpn. 81, 125002 (2012).
5. S. Li, H. Yang, D. L. Feng, Z. Y. Wang, J. Tao, X. X. Ding, and H. H. Wen, Sci. China Phys. Mech. Astron. 56, 2019 (2013).
6. H. Usui, K. Suzuki, and K. Kuroki, Phys. Rev. B 86, 220501 (2012).
7. H. Usui and K. Kuroki, Nov. Supercond. Mater. 1, 50 (2015).
8. K. Hoshi, H. Arima, N. Kataoka, M. Ochi, A. Yamashita, A. D Visser, T. Yokoya, K. Kuroki, Y. Mizuguchi. J. Phys. Soc. Jpn. 92, 054704 (2023).
9. Y. Mizuguchi, A. Miura, J. Kajitani, T. Hiroi, O. Miura, K. Tadanaga, N. Kumada, E. Magome, C. Moriyoshi, Y. Kuroiwa, Sci. Rep., 5, 14968 (2015).
10. J. Xing, S. Li, X. Ding, H. Yang, and H. H. Wen, Phys. Rev. B 86, 214518 (2012).
11. R. Jha, A. Kumar, S. K. Singh, and V. P. S. Awana, J. Supercond. Nov. Magn. 26, 499 (2012).
12. S. Demura, Y. Mizuguchi, K. Deguchi, H. Okazaki, H. Hara, T. Watanabe, S. J. Denholme, M. Fujioka, T. Ozaki, H. Fujihisa, Y. Gotoh, O. Miura, T. Yamaguchi, H. Takeya, and Y. Takano, J. Phys. Soc. Jpn. 82, 033708 (2013).
13. D. Yazici, K. Huang, B. D. White, A. H. Chang, A. J. Friedman, and M. B. Maple, Phil. Mag. 93, 673 (2012).
14. J. Kajitani, T. Hiroi, A. Omachi, O. Miura, and Y. Mizuguchi, J. Phys. Soc. Jpn. 84, 044712 (2015).
15. Y. Fang, D. Yazici, B. D. White, and M. B. Maple, Phys. Rev. B 91, 064510 (2015).
16. I. Jeon, D. Yazici, B. D. White, A. J. Friedman, and M. B. Maple, Phys. Rev. B 90, 054510 (2014).
17. T. Okada, H. Ogino, J. Shomoyama, and K. Kishio, Appl. Phys. Express 8, 023102 (2015).
18. D. Yazici, K. Huang, B. D. White, I. Jeon, V. W. Burnett, A. J. Friedman, I. K. Lum, M. Nallaiyan, S. Spagna, and M. B. Maple, Phys. Rev. B 87, 174512 (2013).

19. H. Kotegawa, Y. Tomita, H. Tou, H. Izawa, Y. Mizuguchi, O. Miura, S. Demura, K. Deguchi, and Y. Takano, J. Phys. Soc. Jpn. 81, 103702 (2012).
20. K. Deguchi, Y. Mizuguchi, S. Demura, H. Hara, T. Watanabe, S. J. Denholme, M. Fujioka, H. Okazaki, T. Ozaki, H. Takeya, T. Yamaguchi, O. Miura, and Y. Takano, EPL 101, 17004 (2013).
21. C. T. Wolowiec, D. Yazici, B. D. White, K. Huang, and M. B. Maple, Phys. Rev. B 88, 064503 (2013).
22. S. Demura, K. Deguchi, Y. Mizuguchi, K. Sato, R. Honjyo, A. Yamashita, T. Yamaki, H. Hara, T. Watanabe, S. J. Denholme, M. Fujioka, H. Okazaki, T. Ozaki, O. Miura, T. Yamaguchi, H. Takeya, and Y. Takano, J. Phys. Soc. Jpn. 84, 024709 (2015).
23. T. Tomita, M. Ebata, H. Soeda, H. Takahashi, H. Fujihisa, Y. Gotoh, Y. Mizuguchi, H. Izawa, O. Miura, S. Demura, K. Deguchi, and Y. Takano, J. Phys. Soc. Jpn. 83, 063704 (2014).
24. T. Hiroi, J. Kajitani, A. Omachi, O. Miura, and Y. Mizuguchi, J. Phys. Soc. Jpn 84, 024723 (2015).
25. E. Paris, Y. Mizuguchi, T. Wakita, K. Terashima, T. Yokoya, T. Mizokawa, and N. L. Saini, J. Phys.: Condens. Matter 30, 455703 (2018).
26. G. M. Pugliese, E. Paris, F. G. Capone, F. Stramaglia, T. Wakita, K. Terashima, T. Yokoya, T. Mizokawa, Y. Mizuguchi, and N. L. Saini, Phys. Chem. Chem. Phys. 22, 22217 (2020).
27. M. Tanaka, T. Yamaki, Y. Matsushita, M. Fujioka, S. J. Denholme, T. Yamaguchi, H. Takeya, and Y. Takano, Appl. Phys. Lett. 106, 112601 (2015).
28. K. Nagasaka, A. Nishida, R. Jha, J. Kajitani, O. Miura, R.Higashinaka, T. D. Matsuda, Y. Aoki, A. Miura, C. Moriyoshi, Y.Kuroiwa, H. Usui, K. Kuroki, and Y. Mizuguchi, J. Phys. Soc. Jpn. 86, 074701 (2017).
29. Y. Mizuguchi, K. Hoshi, Y. Goto, A. Miura, K. Tadanaga, C. Moriyoshi, and Y. Kuroiwa, J. Phys. Soc. Jpn. 87, 023704 (2018).
30. A. Athauda, J. Yang, S. Lee, Y. Mizuguchi, K. Deguchi, Y. Takano, O. Miura, and D. Louca, Phys. Rev. B 91, 144112 (2014).
31. A. Athauda and D. Louca. J. Phys. Soc. Jpn. 88, 041004 (2019).
32. E. Paris, Y. Mizuguchi, M. Y. Hacisalihoglu, T. Hiroi, B. Joseph, G. Aquilanti, O. Miura, T. Mizokawa, and N. L. Saini, J. Phys.: Condens. Matter 29, 145603 (2017).
33. E. Paris, Y. Mizuguchi, T. Wakita, K. Terashima, T. Yokoya, T. Mizokawa, and N. L. Saini, J. Phys.: Condens. Matter 30 455703 (2018).

34. X. Wan, H. C. Ding, S. Y. Savrasov, and C. G. Duan, Phys. Rev. B 87, 115124 (2013).
35. T. Yildirim, Phys. Rev. B 87, 020506 (2013).
36. J. Kajitani, R. Sagayama, H. Sagayama, K. Matsuura, T. Hasegawa, R. Kumai, Y. Murakami, M. Mita, T. Asano, R. Higashinaka, T. D. Matsuda, and Y. Aoki, J. Phys. Soc. Jpn. 90, 103601 (2021).
37. H. F. Zhai, Z. T. Tang, H. Jiang, K. Xu, K. Zhang, P. Zhang, J. K. Bao, Y. L. Sun, W. H. Jiao, I. Nowik, I. Felner, Y. K. Li, X. F. Xu, Q. Tao, C. M. Feng, Z. A. Xu, and G. H. Cao, Phys. Rev. B 90, 064518 (2014).
38. J. Lee, M. B. Stone, A. Huq, T. Yildrim, G. Ehlers, Y. Mizuguchi, O. Miura, Y. Takano, K. Deguchi, S. Demura, and S. H. Lee, Phys. Rev. B, 87, 205134 (2013).
39. A. Omachi, J. Kajitani, T. Hiroi, O. Miura, and Y. Mizuguchi, J. Appl. Phys. 115, 083909 (2014).
40. A. Nishida, H. Nishiate, C. H. Lee, O. Miura, and Y. Mizuguchi, J. Phys. Soc. Jpn. 85, 074702 (2016).
41. Y. Mizuguchi, A. Omachi, Y. Goto, Y. Kamihara, M. Matoba, T. Hiroi, J. Kajitani, and O. Miura, J. Appl. Phys. 116, 163915 (2014).
42. A. Nishida, O. Miura, C. H. Lee, and Y. Mizuguchi, Appl. Phys. Express 8, 111801 (2015).
43. Y. Mizuguchi, A. Miura, A. Nishida, O. Miura, K. Tadanaga, N. Kumada, C. H. Lee, E. Magome, C. Moriyoshi, and Y. Kuroiwa, J. Appl. Phys. 119, 155103 (2016).
44. C. H. Lee, A. Nishida, T. Hasegawa, H. Nishiate, H. Kunioka, S. Ohira-Kawamura, M. Nakamura, K. Nakajima, and Y. Mizuguchi, Appl. Phys. Lett. 112, 023903 (2018).
45. H. M. Rietveld, Acta Crys. 20, 508 (1966).
46. F. Izumi and K. Momma, Solid State Phenom. 130, 15 (2007).
47. K. Momma and F. Izumi, J. Appl. Crystallogr. 41, 653 (2008).
48. S. Kawaguchi, M. Takemoto, K. Osaka, E. Nishibori, C. Moriyoshi, Y. Kubota, Y. Kuroiwa, and K. Sugimoto, Rev. Sci. Instrum. 88, 085111 (2017).
49. K. Wakiya, T. Onimaru, S. Tsutsui, T. Hasegawa, K. T. Matsumoto, N. Nagasawa, A. Q. R. Baron, N. Ogita, M. Udagawa, and T. Takabatake, Phys. Rev. B 93, 064105 (2016).
50. K. Umeo, K. Suekuni, T. Takabatake, and E. Nishibori, Phys. Rev. B 102, 100302 (2020).
51. N. Nakamura, R. Higashinaka, Y. Aoki, H. Sato, T.D. Matsuda, Solid State Commun. 363, 115098 (2023).
52. Y. Ikeuchi, H. Takatsu, C. Tassel, C. M. Brown, T. Murakami, Y. Matsumoto, Y. Okamoto, and H. Kageyama, Inorg. Chem. 58, 6790 (2019).

53. A. P. Ramirez, G. R. Kowach, Phys. Rev. Lett. 80, 4903 (1998).
54. T. Berry, S. R. Parkin, and T. M. McQueen, Phys. Rev. Materials 5, 114401 (2021).
55. M. Bouvier, P. Lethuillier, and D. Schmitt, Phys. Rev. B 43, 137 (1991).
56. T. M. Seixas, M. A. Salgueiro da Silva, O. F. de Lima, J. Lopez, H. F. Braun, and G. Eska, J. Phys.: Condens. Matter 22, 136002 (2010).
57. F. I. Abbas, H. Arima, M. R. Kasem, Y. Watanabe, T. Hasegawa, C. H. Lee, A. Yamashita, and Y. Mizuguchi, Appl. Phys. Express, Accepted, (2023). DOI: 10.35848/1882-0786/ad0ba6.
58. K. Hoshi, S. Sakuragi, T. Yajima, Y. Goto, A. Miura, C. Moriyoshi, Y. Kuroiwa, Y. Mizuguchi, Condens. Matter 5, 81 (2020).
59. N. Kase, Y. Terui, T. Nakano, and N. Takeda, Phys. Rev. B 96, 214506 (2017).
60. J. Bardeen, L. Cooper, and J. R. Schrieffer, Phys Rev. 108, 1175 (1957).
61. E. Grüneisen, Annalen der physik, 344, 257 (1912).
62. D. K. C. MacDonald and S. K. Roy, Phys. Rev. 97, 673 (1955).
63. F. I. Abbas, A. Yamashita, K. Hoshi, R. Kiyama, Md. R. Kasem, Y. Goto, and Y. Mizuguchi, Appl. Phys. Express 14, 071002 (2021).
64. F. I. Abbas, K. Hoshi, Y. Nakahira, M. Yoshida, A. Yamashita, H. Ito, A. Miura, C. Moriyoshi, C. H. Lee, and Y. Mizuguchi, J. Phys. Soc. Jpn. 92, 014703 (2023).
65. F. I. Abbas, K. Hoshi, A. Yamashita, Y. Nakahira, Y. Goto, A. Miura, C. Moriyoshi, Y. Kuroiwa, K. Terashima, R. Matsumoto, Y. Takano, and Y. Mizuguchi, J. Phys. Soc. Jpn. 91, 074706 (2022).
66. A. Mohamad, Y. Ohishi, H. Muta, K. Kurosaki, and S. Yamanaka, J. Nuclear Sci. Technol. 55, 1141 (2018).
67. A. Nomura, S. Choi, M. Ishimaru, A. Kosuga, T. Chasapis, S. Ohno, G. J. Snyder, Y. Ohishi, H. Muta, S. Yamanaka, and K. Kurosaki, ACS Appl. Mater. Interfaces 10, 43682 (2018).
68. R. Jha, A. Kumar, S. K. Singh, and V. P. S. Awana, J. Supercond. Novel Magn. 26, 499 (2013).
69. R. Jha, A. Kumar, S. K. Singh, and V. P. S. Awana, J. Appl. Phys. 113, 056102 (2013).
70. R. Higashinaka, T. Asano, T. Nakashima, K. Fushiya, Y. Mizuguchi, O. Miura, T. D. Matsuda, and Y. Aoki, J. Phys. Soc. Jpn. 84, 023702 (2015).

Publication list

(1) F. I. Abbas, H. Arima, M. R. Kasem, Y. Watanabe, T. Hasegawa, C. H. Lee, A. Yamashita, and Y. Mizuguchi, “Stabilization of Bi vibration along *c*-axis in BiS_2-based layered compounds La(O,F)Bi(S,Se)$_2$ by Se substitution”, Appl. Phys. Express, Accepted, (2023). DOI: 10.35848/1882-0786/ad0ba6.

(2) F. I. Abbas, K. Hoshi, Y. Nakahira, M. Yoshida, A. Yamashita, H. Ito, A. Miura, C. Moriyoshi, C. H. Lee, Y. Mizuguchi, "Estimation of Grüneisen Parameter of Layered Superconductor $LaO_{0.5}F_{0.5}BiS_{2-x}Se_x$ (x = 0.2, 0.4, 0.6, 0.8 1.0)", J. Phys. Soc. Jpn. 92, 014703 (2023), DOI: 10.7566/JPSJ.92.014703.

(3) F. I. Abbas, K. Hoshi, A. Yamashita, Y. Nakahira, Y. Goto, A. Miura, C. Moriyoshi, Y. Kuroiwa, K. Terashima, R. Matsumoto, Y. Takano, Y. Mizuguchi, "Lattice Anharmonicity in BiS_2-Based Layered Superconductor RE(O,F)BiS_2 (RE = La, Ce, Pr, Nd)", J. Phys. Soc. Jpn. 91, 074706 (2022), DOI: 10.7566/JPSJ.91.074706.

(4) F. I. Abbas, Y. Nakahira, A. Yamashita, Md. R. Kasem, M. Yoshida, Y. Goto, A. Miura, K. Terashima, R. Matsumoto, Y. Takano, C. Moriyoshi, Y. Mizuguchi, "Estimation of the Grüneisen Parameter of High-EntropyAlloy-Type Functional Materials: The Cases of $REO_{0.7}F_{0.3}BiS_2$ and MTe", Condens. Matter 7, 34 (2022), DOI: 10.3390/condmat7020034.

(5) F. I. Abbas, A. Yamashita, K. Hoshi, R. Kiyama, Md. R. Kasem, Y. Goto, Y. Mizuguchi, "Investigation of lattice anharmonicity in thermoelectric $LaOBiS_{2-x}Se_x$ through Grüneisen parameter", Appl. Phys. Express 14, 071002 (2021), DOI: 10.35848/1882-0786/ac06b0.

APPENDIX

A1 Superconductivity

History of superconductivity and material discovery

Kamerlingh Onnes, a Dutch physicist, made the discovery of superconductivity in 1911 [A1]. In 1913, he was given the Nobel Prize in Physics for his study of low-temperature physics, which led to his being recognized as a pioneer in the field. Kamerlingh Onnes found that the electrical resistance of a mercury (Hg) wire vanishes almost immediately at temperatures below 4 K [A1]. Soon after, he realized that a superconducting material can return to its normal state if either a sufficiently strong current is delivered through it or a sufficiently strong magnetic field is provided. Both of these conditions were met. It was believed for a very long time that superconductors have the same qualities as conventional materials, with the distinction that they do not have any electrical resistance. The theory was demolished in 1933 when it was discovered that a superconductor has a high diamagnetic permeability, meaning that it is strongly repelled by a magnetic field and prefers to expel it. The Meissner effect [A2] is a phenomenon that is seen in superconductors and has a significant impact on their properties. 1934 saw the development of a hypothesis concerning the electromagnetic properties of superconductors as a direct result of the discovery of the phenomenon [A3]. This theory made a prediction about the existence of an electromagnetic penetration depth, and in 1939 [A4], that prediction was experimentally confirmed for the first time. In 1950, it was conclusively proven for the first time that a theory of superconductivity must account for the fact that free electrons in a crystal are influenced by the lattice vibrations and atom vibrations that shape the crystal structure [A5, A6]. This was a significant step forward in proving that a theory of superconductivity must account for all of the factors that determine the crystal structure. During research on the thermal conductivity of superconductors that was carried out in 1953, it was found that the distribution of free electron energies in a superconductor is not uniform and that there is a separation between them that is referred to as the energy gap [A7].

Since 1911, researchers have identified several distinct types of superconductors [A1]. In 1986, Bednorz and Müller discovered that layered superconductors based on copper oxide

could be produced [A8]. Researchers have discovered a variety of different Cu-oxide superconductors.

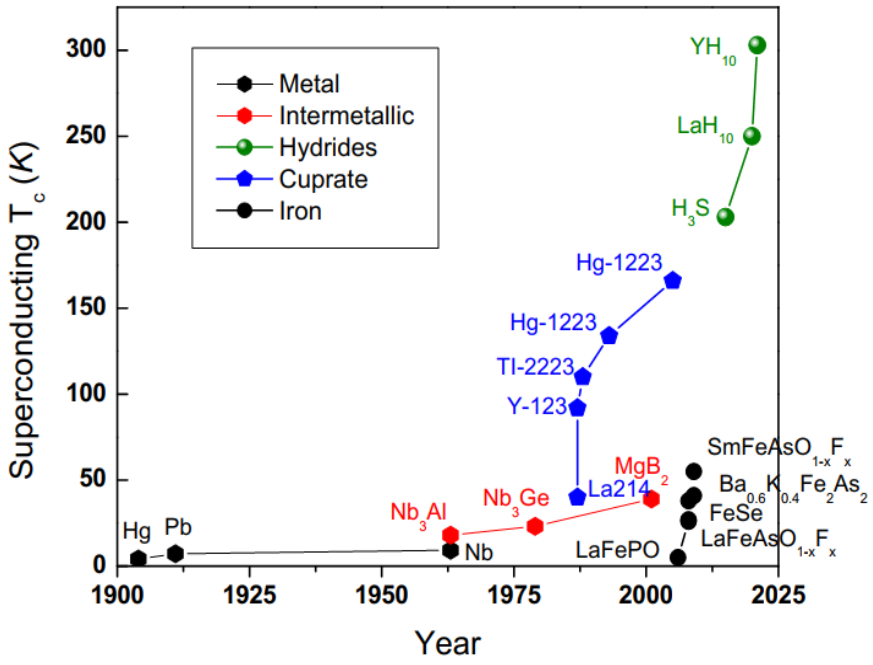

Fig. A1.: Schematic history of superconductors since 1911 (T_c vs Year).

In Fig. A1, the critical temperatures (T_c) of typical materials are shown. The T_c of Cu-oxide superconductors is greater than the boiling temperature of liquid nitrogen (77 K). In addition to this, a Fe-based superconductor with a T_c higher than 50 K was discovered [A9]. Recently, researchers have shown that superconductors based on hydrogen-rich compositions (superhydrides) can achieve T_c values that are closer to those of ambient temperature [A9-A14].

Basic properties of superconductors

In comparison to other types of materials, superconducting materials exhibit several unusual behaviors. Those behaviors are observed below T_c. Typical properties are explained in the following paragraphs. The figures in this part were prepared after "Introduction text book on superconductivity" by Tinkham [A15].

Zero resistivity

Electrical resistivity (ρ) of metals decreases with decreasing temperature. In the case of a superconducting material, ρ suddenly drops to zero at T_c. A schematic image is shown in Fig. A2.

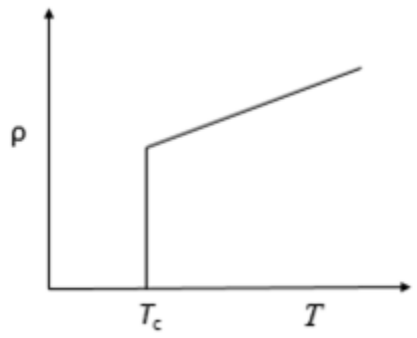

Fig. A2: Zero resistivity below T_c.

Meissner effect

The electrical conductivity of a substance can be defined as when it is in its normal state,

$$\sigma = \frac{j}{E} \qquad (1)$$

where j is the electrical current and E is the electric field.

If σ has an infinite value, then $E = 0$.

According to Maxwell's equation [A16],

$$\nabla \times \boldsymbol{E} = - \frac{d\boldsymbol{B}}{dt} \qquad (2)$$

or, B = constant (when $E = 0$)

We suppose that B is equal to zero when talking about a superconducting state, which occurs when the temperature is below T_c. After that, a magnetic field was applied to the sample, and it was discovered that the magnetic field did not penetrate inside the sample. The name given to this type of conduct is "Meissner effect.", where perfect diamagnetism is observed.

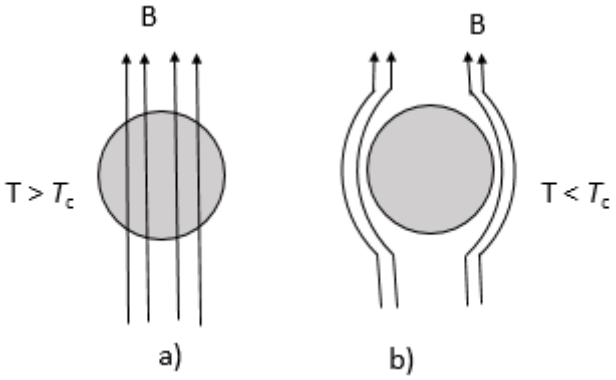

Fig. A3: a) penetration of B at normal state and b) below T_c, applied field is expelled.

W. Meissner and R. Ochsenfeld made the discovery that this quality existed in the year 1933 [A7]. They found that superconducting elements such as lead had this behavior. They discovered that below the critical temperature, the superconductor gives forth a very feeble magnetic field. On the other hand, a strong field can eliminate the superconducting property of a material, leaving it to act similarly to a regular substance.

Josephson effect

A graduate student named Brian Josephson published a theory in 1962 that explained how supercurrent tunneling between superconductors could occur even when those superconductors were physically separated from one another by an insulator. The cooper pairs are responsible for the occurrence of this supercurrent.

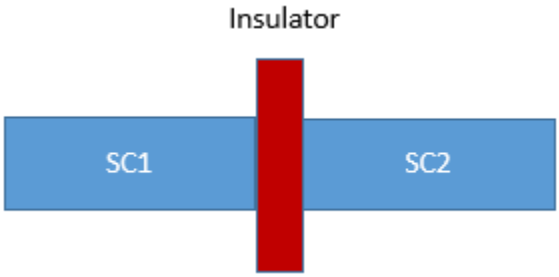

Fig. A4: Josephson Junction between two superconductors (SC1 and SC2).

The quantum tunneling effect of the Cooper pair electrons is responsible for the flow of current across the thin, insulating Josephson junction (Fig. A4) when the voltage is zero. Simply put, t thickness that is permitted is just a few microns. A layer that is too thick would make tunneling more difficult. When there is no voltage across the junction, there is a maximum value for the amount of current that can flow through it. For a Josephson junction, this current is referred to as the critical current. Even though the critical current is always the same, it can change depending on the temperature, the superconducting materials present, and the magnetic flux that is being applied.

When there is no applied voltage, then the direct current (DC) is $I_{sc} = I_c \sin(\theta_1 - \theta_2)$. Hence, I_c is the critical current, and $(\theta_1 - \theta_2)$ is the phase difference of supercurrent between two superconductors. If a finite DC voltage, V is applied then alternating current (AC) oscillates with frequency, $\omega = 2eV/\hbar$, where, Plank constant, $\hbar = 1.054 \times 10^{-34}$ Js. This theory was very accurate and later it was verified. He won Nobel prize in 1973 for his work.

Superconducting transition

Critical temperature (transition temperature)

At T_c, the electrical resistivity becomes zero as explained with a schematic image in the above part. Figure 5 shows the example of resistivity experiment. The temperature at which the ρ begins to drop is denoted as T_c^{onset}, and the temperature at which the ρ reaches zero is T_c^{zero} (Fig. A5).

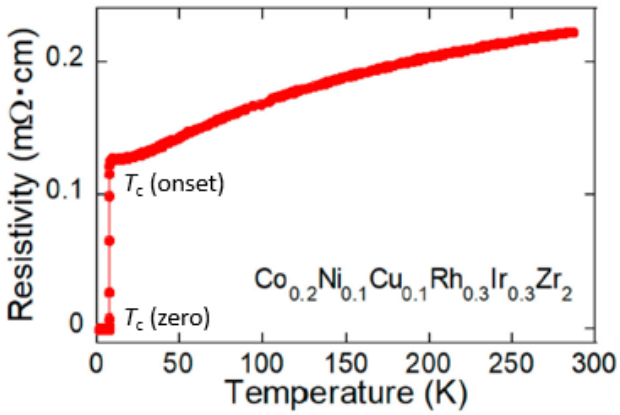

Fig. A5: Temperature dependent electrical resistivity.

In magnetization data, the value of T_c is defined as the temperature where diamagnetic responses appear. Another critical temperature, irreversibility temperature (T_c^{irr}), is defined as the temperature at which field cooling (FC) and zero field cooling are equivalent. (ZFC) are separated from each other (Fig.A6). In many cases, T_c^{zero} and T_c^{irr} becomes similar value because those are related to the emergence of supercurrent.

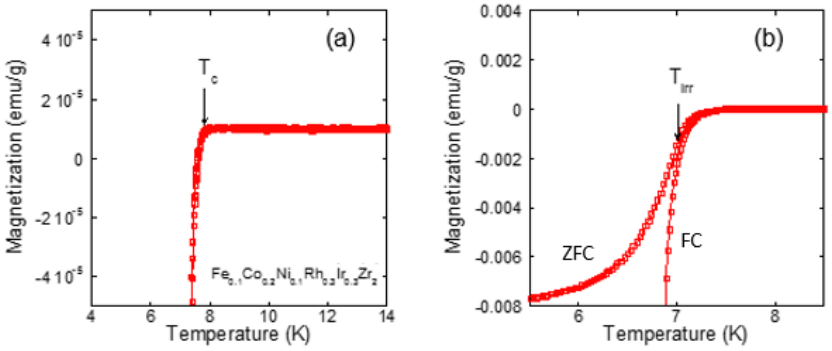

Fig. A6: Temperature dependent magnetization.

Type-I superconductor

Within a superconducting material, it was found that the Meissner effect prevented any magnetic field from penetrating the interior of the substance. It occurs when the magnetic field that is applied is not very strong, and the superconducting condition is lost when the applied field is strong enough to penetrate inside the superconductor. At a specific magnetic field, there is a transition point where the superconducting states disappear as shown in Fig. A7. Above that value, the sample is in a normal state, while below that point, the sample is in a superconducting state. This location is referred to as the critical field (H_c) point. The critical field is characterized by the following: [A15]

$$H_c(T) = H_c(0)\,[1 - (T/T_c)^2] \qquad (3)$$

The term "type-I superconductor" refers to the properties exhibited by substances that behave in such a way. Because of the sudden change in behavior in response to an increase in the magnetic field, this material is also known as a soft superconductor. Superconductors in type-I include Hg, Pb, Zn, and others.

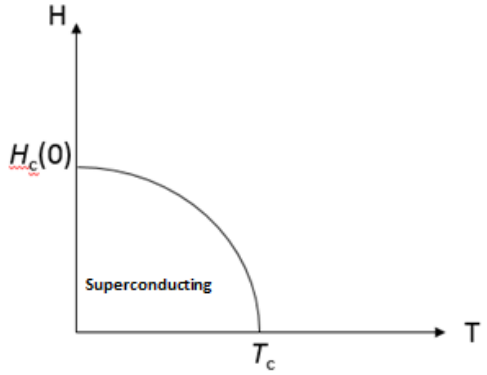

Fig. A7: Critical field of type-I superconductor.

Type-II superconductor

Most superconductors are a type-II superconductor. The important features are the presence of lower and upper critical fields (H_{c1} and H_{c2}). When $H < H_{c1}$, [A2] the Meissner effect emerges, where the magnetic fields are expelled. On the other hand, when $H_{c1} < H < H_{c2}$, a mixed state is observed (Fig. A8). In this region, magnetic fluxes are incorporated in the superconductor. When the sample is subjected to an applied field that is strong enough to overcome the limit of H_{c2}, the sample returns to its normal state. Alloys such as Pb-In [A19]

and NbTi, [A19] and compounds such as Nb_3Sn [A20] and layered superconductors, and dirty samples exhibit type-II characteristics in most cases.

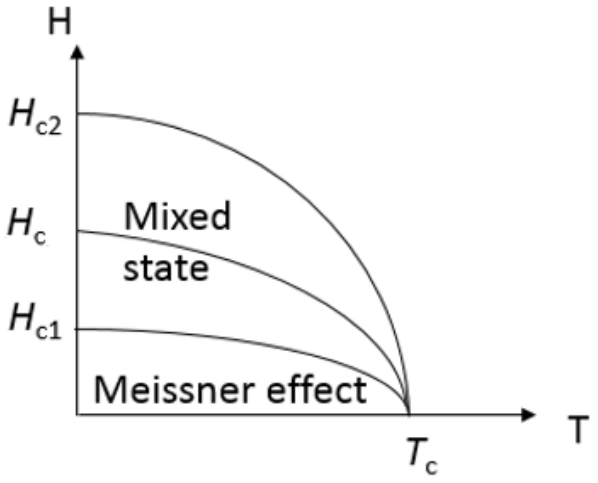

Fig. A8: Critical field of type-II superconductor.

Critical current

Above the current (density) limit, superconductivity is suppressed. The value in question is referred to as the critical current density (J_c). Within the superconductor, magnetic flux can be seen to enter in the form of vortices in the region shown by the notation $H_{c1} < H < H_{c2}$. Each vortex is a quantum flux, denoted by the symbol, $\boldsymbol{\Phi}$ which equals 2.07×10^{-15} Wb. The energy level in that region is higher than the energy level in the H_{c1} zone, and supercurrents surround the vortices in that region. These vortices push against one another, creating a uniform triangular lattice that minimizes energy loss and is held in place by a pinning force denoted by the symbol f_P. Each vortex is subjected to something known as the Lorentz force $\boldsymbol{J} \times \boldsymbol{B}$ as a consequence of the current density J. Vortices will begin to move and produce resistance if this force is larger than the force that is anchoring them in place. The term "flux-flow resistance" can also be used to refer to this resistance. In spite of the fact that this resistance is extremely low, the state of the material is no longer that of a superconductor. The formula for determining the critical current density in terms of the pinning force is as follows: $J_c = f_p/B$, where B refers to the magnetic field that is being applied. The critical current density varies with the magnetic field that is being applied as well as the temperature.

High-T_c superconductors

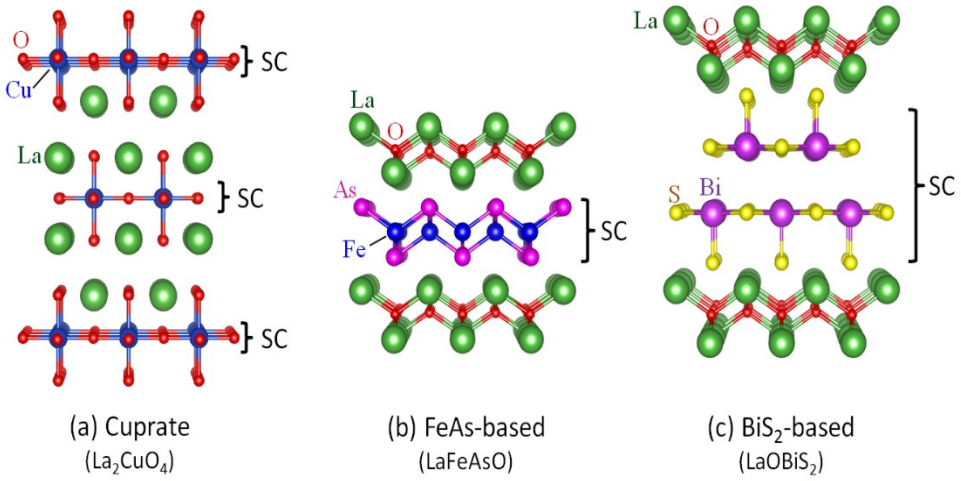

Fig. A10: Schematic Crystal structure of layered superconducting materials.

After the discovery of the first Cu-oxide superconductor [A8], high-T_c superconductivity has been observed in various layered compounds. Cu-oxide (cuprate) superconductors [A21-A26] have T_cs exceeding 77 K, which is the boiling temperature of nitrogen. The essential crystal structure is CuO_2 planes. Basically, parent phases of Cu-oxide superconductors are a antiferromagnetic Mott insulator, and carrier doping suppresses the Mott insulating states and antiferromagnetic ordering, and high- T_c superconductivity is induced. The pairing mechanism is basically understood as spin-fluctuation scenario, where antiferromagnetic spin fluctuation helps electrons to form pairs. Then, d-wave superconducting gap is realized.

In 2001, superconductivity in MgB_2 with a T_c of 39 K was discovered [A27]. MgB_2 is a layered compound, but it does not exhibit magnetic ordering, and the characteristics are different from those of Cu-oxide superconductors [A25, A26]. The pairing mechanism is explained by conventional phonon-mediated scenario, particularly with phonons of B in MgB_2.

In 2006, superconductivity in LaFePO was reported [A28]. It surprised researchers in the field of superconductivity because of the superconducting layers mainly composed of Fe, which is a typical magnetic element. In 2008, high-T_c superconductivity was observed in $LaFeAsO_{1-x}F_x$ ($T_c = 26$ K) [A29], and T_c of the family exceeded 50 K by replacing La by smaller rare earth ions (namely, by chemical pressure effect) [A30-A33]. The parent phases of the Fe-based superconductors are an antiferromagnetic metal. For example, in $LaFeAsO_{1-x}F_x$, partial F substitution for the O site suppresses antiferromagnetism, and superconductivity is induced.

Although the above F substitution dopes electron carriers in the FeAs layers [A32], similar phenomena, suppression of magnetism and emergence of superconductivity, is observed by chemical pressure effects and physical pressure effects [30]. On the pairing mechanisms, the importance of both spin fluctuations and orbital fluctuations have been suggested. In addition, gap symmetry depends on the crystal structure [A31].

In 2015, superconductivity of H_3S with T_c = 203 K under extremely high pressures was reported [A34]. Basically, the mechanism of superconductivity in hydrides are phonon-mediated mechanism with high phonon energy of H. High- T_c superconductivity has been predicted by conventional phonon mechanisms, but realization of the H-rich materials under high pressures was challenging. Recent development of diamond-anvil cell solved the difficulty. The important feature is the phonon-mediated conventional pairing that was confirmed by the isotope effect.

A2. Rietveld refinement

Rietveld refinement is a method for the analysis of X-ray (or neutron) diffraction patterns as well as to the characterization of crystalline materials. It can be used for both single and multiple phases. Hugo Rietveld is credited with being the one who first conceived of the idea in the 1960s [A35]. According to the obtained XRD patterns, various variable parameters are refined to reproduce the peak height, shape, broadness, peak position, etc. As a result of the refinements, we can confirm the phase purity including the population of the main phase, and the structural parameters including atomic coordinates, occupations, and atomic displacement parameters, which are described as *B* or *U*.

B and *U* factors

The atomic vibration (thermal motion of the constituent atoms) leads to a decrease in X-ray scattering. The atomic displacement can be considered as either temperature-dependent (dynamic) atomic vibration within the crystal lattice or temperature-independent (static) structural disorder. The atomic vibrations in isotropic displacement are evenly distributed in all directions. On the other hand, when anisotropic displacement is present in the material with an anisotropic crystal structure, the vibrations occur in the specific directionss. The Debye-Waller factor is used as a measure of the decrease in the scattering factor. The following is the expression for the factor.

$$T(\mathbf{h}) = \exp\left[-8\pi^2 \langle u_{\mathbf{h}}^2 \rangle (\sin^2\theta)/\lambda^2\right] \qquad (1)$$

where $u_{\mathbf{h}}$ is the projection of the atomic displacement u on the direction of diffraction vector **h**, θ is the X-ray scattering angle, and λ is the corresponding wavelength of the X-ray.

Thermal factor constraints can be expressed in terms of the invariance of the thermal factor tensor matrix, **U**, with respect to the point-group symmetry operations of the crystal site,

$$\mathbf{U} = \mathbf{h}^{\mathbf{T}}\mathbf{U}\mathbf{h} \qquad (2)$$

The mean-square displacement (MSD) is defined in terms of an anisotropic displacement parameter.

$$T(\mathbf{h}) = \exp[-2\pi^2 \mathbf{h}^{\mathbf{T}}\mathbf{U}\mathbf{h}] \qquad (3)$$

The following is the displacement parameter tensor.

$$\boldsymbol{U} = \begin{bmatrix} U_{11} & U_{12} & U_{13} \\ U_{12} & U_{22} & U_{23} \\ U_{13} & U_{23} & U_{33} \end{bmatrix} \quad (4)$$

where $\underline{U_{ij}}$ has the dimension of square of length (typically Å^2). In the case of the isotropic factors, only diagonal values, U_{11}, U_{22}, U_{33}, are considered. For the case of anisotropic factor, all the U_{ij} are considered. In this study, we used U_{11} and U_{33} in the introduction part.

If the atomic displacement is isotropic, the Debye-Waller factor (1) could be described as the following.

$$T(|\mathbf{h}|) = \exp[-8\pi^2 <\mathbf{u}^2> (\sin^2\theta)/\lambda^2] \quad (5)$$

where |**h**| is the magnitude of **h.** The MSD parameter is directly linked to the *B* factor with the following relation.

$$\boldsymbol{B = 8\pi^2 <u^2>}$$

A3. Thermoelectric materials

Converting waste heat into electricity is critical for growing renewable energy sources and lowering fossil fuel and greenhouse gas emissions [A36]. Engines fueled by combustion produce residual thermal energy. Vehicle movement and accessories use just 21% of fuel energy, but exhaust gas accounts for 38%. Efficiency is what drives the use of thermoelectric materials (TE). Many years ago, metal thermocouples used the thermoelectric Seebeck effect to measure temperature [A37]; Seebeck coefficient (S) is one of the key parameters for thermoelectric performance. For energy conversion, to obtain a larger electric power, a larger power factor, which is defined as $PF = S^2\sigma$, is needed (σ is electrical conductivity). Because those two parameters generally have trade-off relationship; if electrical conductivity is enhanced, the absolute value of Seebeck coefficient decreases typically in semiconductors. Furthermore, to enhance the thermoelectric conversion performance, low thermal conductivity is needed because a larger temperature gradient is needed. To evaluate the behavior of TE materials, we use the figure of merit (ZT) of the TE material.

Figure of merit

Altenkirch first proposed the figure of merit in 1912 [A38,A39], demonstrating that good thermoelectric materials maintain a broad temperature gradient, have high electrical conductivity, and have poor thermal conductivity at junctions. Ioffe established the Z = [PF]/ $\kappa = S^2\sigma/\kappa$ figure of merit in 1957 to evaluate thermoelectric material efficiency [A40]. Dimensionless merit is usually (1).

$$ZT = [PF]\frac{T}{\kappa} = \frac{S^2\sigma T}{\kappa} \qquad (1)$$

In addition to the correlation between S and σ, the electronic conductivity and the thermal conductivity (carrier thermal conductivity) are coupled. Therefore, one of the promising strategies for producing a high-ZT material is reduction of lattice thermal conductivity in materials where PF is optimized.

Reference for Appendix

A1. H. K. Onnes, Akad. van Wetenschappen (Amsterdam) **14**, 113, 818 (1911).

A2. W. Meissner and R. Ochsenfeld, Naturwiss. **21**, 787 (1933).

A3. Burton, E. F., Wilhelm, J. O. and Misener, A. D. Trans. Roy. Soc. Can. **28**, III, 65 (1934).

A4. Superconductivity of thin films. Part I. Mercury. Proc. R. Soc. Lond. A, **172**, 540-558 (1939).

A5. A. B. Pippard, Field variation of the superconducting penetration depth. Prog. R. Soc. A 203, 210–223 (1950).

A6. V. L. Ginzburg, L. D. Landau, On the theory of superconductivity. Zh. Eksp. Teor. Fiz. **20,** 1064–1082, (1950).

A7. D. Shoenberg, Physica, **19**, 788-790 (1953).

A8. J. G. Bednorz, and K. A. Müeller, Z. Phys. B. 64 (2): 189 (1986).

A9. Kamihara, T. Watanabe, M. Hirano, H. Hosono, J. Am. Chem. Soc. **130**, 11, 3296–3297 (2008).

A10. N. W. Ashcroft, Phys. Rev. Lett. 92, 187002 (2004).

A11. A. P. Drozdov1, M. I. Eremets, I. A. Troyan, V. Ksenofontov and S. I. Shylin, Nature **525**, 73–76 (2015).

A12. H. Wang, J. S. Tse, K. Tanaka,T. Iitaka, and Y. Ma Proc. Natl Acad. Sci. USA **109**, 6463 (2012).

A13. P. Kong, V. S. Minkov, M. A. Kuzovnikov, A. P. Drozdov, S. P. Besedin, S. Mozaffari, L. Balicas, F. Fedorovich Balakirev, V. B. Prakapenka, S. Chariton, D. A. Knyazev, E. Greenberg and M. I. Eremets, Nat. Commun **12,** 5075 (2021).

A14. F. Peng, Y. Sun, C. J. Pickard, R. J. Needs, Q. Wu, and Y. Ma Phys. Rev. Lett. **119**, 107001 (2017).

A15. M. Tinkham, Introduction to superconductivity, McGraw-Hill New York (1975).

A16. N. W. Ashcroft, and N. D. Mermin, Solid State Physics, Cengage Learning, India (1976).

A17. Y. Mizuguchi, M.R. Kasem and T.D. Matsuda, Mat. Res. Lett., **9:3**, 141 (2021).

A18. M. R. Kasem, A. Yamashita, Y. Goto, T. D. Matsuda, and Y. Mizuguchi, J. Mater Sci **56**, 9499 (2021).

A19. G. Fischer, and K. Maki. Phys. Rev. 176, 581 (1968).

A20. A. Echarri, M. Spadoni, Cryogenics **11**, 274-284 (1971).

A21. M. K. Wu, J. R. Ashburn, C. J. Torng, P. H. Hor, R. L. Meng, L. Gao, Z. J. Huang, Y. Q. Wang, and C. W. Chu Phys. Rev. Lett. **58**, 908 (1987).

A22. H. Maeda, Y. Tanaka, M. Fukutomi, and T. Asano, Jpn. J. Appl. Phys. **27** L209 (1988).

A23. S. S. P. Parkin, V. Y. Lee, E. M. Engler, A. I. Nazzal, T. C. Huang, G. Gorman, R. Savoy, and R. Beyers, Phys. Rev. Lett. **60**, 2539(1988).

A24. A. Schilling, M. Cantoni, J. D. Guo, H. R. Ott, Nature **363**, 56 (1993).

A25. M. Monteverde, C. Acha, M. Núñez-Regueiro, D. A. Pavlov, K. A. Lokshin, S. N. Putilin and E. V. Antipov, EPL **72** 458 (2005).

A26. J. Nagamatsu, N. Nakagawa, T. Muranaka, Y. Zenitani, and J. Akimitsu, Nature **410**, 63 (2001).

A27. D. G. Hinks, H. Claus, & J. D. Jorgensen. Nature **411**, 457 (2001).

A28. Y. Kamihara, H. Hiramatsu, M. Hirano, R. Kawamura, H. Yanagi, T. Kamiya, and H. Hosono, J. Am. Chem. Soc., 128, 31, 10012 (2006).

A29. Y. Kamihara, T. Watanabe, M. Hirano, and H. Hosono, J. Am. Chem. Soc., 130, 11, 3296 (2008).

A30. C. Wang, L. Li, S. Chi, Z. Zhu, Z. Ren, Y. Li, Y. Wang, X. Lin, Y. Luo, S. Jiang, X. Xu, G. Cao and Z. Xu, Europhys. Lett. 83, 67006 (2008).

A31. X. Lin, C. Shen, C. Lv, J. Miao, H. Tan, G. Cao and Z. Xu ; J. Phys.: Cond. Matt., 23, 46 (2011).

A32. K. Kaneyasu, R. Sakagami, M. Matoba and Y. Kamihara; JJAP, 58, 030911 (2019).

A33. Y. Yamamoto, H. Yamaoka, T. Kawai, M. Yoshida, J. Yamaura, K. Ishii, S. Onari, T. Uozumi, A. Hariki, M. Taguchi, K. Kobayashi, J. Lin, N. Hiraoka, H. Ishii, K. Tsuei, H. Okanishi, S. Iimura, S. Matsuishi, H. Hosono and J. Mizuki. J. Phys.: Cond. Matt., **33**, 25 (2021).

A34. A. P. Drozdov, M. I. Eremets, I. A. Troyan, V. Ksenofontov & S. I. Shylin. Nature **525**, 73-74 92015).

A35. H. M. Rietveld, Acta Crys. 20, **508** (1966).

A36 G. J. Snyder, E. S. Toberer, Nature Materials, 7 (2008) 105.

A37 G. S. Nolas, J. Poon, M. Kanatzidis, MRS Bulletin, 31 (2006) 199.

A38 E. Altenkirch, Phys. Zeitschrift, 10 (1909) 560.

A39 E. Altenkirch, Phys. Zeitschrift, 12 (1911) 920.

A40 A. F. Ioffe, Semiconductor Thermoelements and Thermoelectric Cooling, Infosearch, London, 1957.

Acknowledgments

To begin, I would like to express my appreciation to the administration of the Tokyo Metropolitan Institution for giving me the chance to participate in this program as part of the Tokyo Metropolitan Fund for City Diplomacy that the institution sponsors. In addition to that, I would like to express my gratitude to my supervisor, Dr. Y. Mizuguchi, for providing me with the opportunity to work on his team. During the time that I was working on my Ph.D., he was an invaluable resource for me in terms of my research. I found his guidance and instructions to be really beneficial.

I would like to thank Dr. Kurita and Dr. Hattori for their efforts as referee of the degree and giving fruitful discussion and suggestions.

I would like to express my gratitude to Dr. Arima for providing insightful feedback on the work I've been doing in the field of research. I'd like to take this opportunity to thank Dr. Yamashita for the consistent support he's given me during my Ph.D. studies, both in terms of his guidance and the laboratory work we've done. In addition, I would like to express my gratitude to both Dr. Hoshi and Dr. Kasem for the invaluable counsel they provided me about the various aspects of my research.

I thank to my present laboratory mates Sawahara, Yoshida, Watanabe, Seshita, Yamanaka, Murakami, Okada, Shimada, Muroi and ex. laboratory mates Kiyama, Katsuno, Morino, Mitobe (Mizuguchi group) who helped me not only in my research work but also my personal issues in last 3.5 years.

I like to thank Dr. Y. Nakahira (QST), Dr. A. Miura (Hokkaido University) too for the support in synchrotron XRD and analysis. I thank Dr. T. Hasegawa (Hiroshima University) and Dr. C. H. Lee (AIST) for the supports in phonon analysis.

Last but not least, I would like to express my appreciation to my wife, Mosume Samad (a doctoral student at Saitama University, Japan, with a MEXT scholarship), my all parents, my younger brother Fieid, my elder sister Dr. Fateha Samad (Professor of RUET), my elder brother Dr. Kamal (Professor of RUET), my friend Mr. Milon (BCS cadar) & Mr. Salahuddin

(University faculty member in Bangladesh), my university junior brother Miraj, and other members of my family who have always encouraged me to finish my education and to take pleasure in my life in Japan despite the COVID pandemic that was going on there.

Fysol Ibna Abbas